Correlations between thermodynamic fluctuations in shock wave/turbulent boundary layer interaction

Ximeng Hou [1,2] Dehao Xu [3] Jianchun Wang [1,2,*] and Shiyi Chen [4,1,2,5,†]

[1]*Department of Mechanics and Aerospace Engineering, Southern University of Science and Technology, Shenzhen 518055, People's Republic of China*

[2]*Guangdong Provincial Key Laboratory of Turbulence Research and Applications, Southern University of Science and Technology, Shenzhen 518055, People's Republic of China*

[3]*Physics of Fluids Group, Max Planck Center for Complex Fluid Dynamics, and J. M. Burgers Centre for Fluid Dynamics, University of Twente, P.O. Box 217, 7500AE Enschede, The Netherlands*

[4]*Eastern Institute for Advanced Study, Ningbo 315200, People's Republic of China*

[5]*State Key Laboratory of Turbulence and Complex Systems, Peking University, Beijing 100871, People's Republic of China*

(Received 18 February 2024; accepted 12 July 2024; published 31 July 2024)

The second moment correlations between thermodynamic fluctuations in incident shock wave/turbulent boundary layer interaction flows at Mach 2.25 are systematically investigated by direct numerical simulation. The concerned fluctuations are those of pressure, entropy, temperature, and density $\{p', s', T', \rho'\}$. Effects of wall temperature and Reynolds number are studied. Kovásznay decomposition is introduced to decompose the fluctuations into acoustic and entropic modes. It is shown that all the six concerned correlations are determined by merely two parameters, which are interpreted as intermodal competition and intermodal correlation, respectively. Accordingly, the flow field is divided into several zones, each with distinct physical properties, to analyze the contributing factors to the correlations. In addition, a model is proposed where the correlations are deemed as functions of the root-mean-square values of thermodynamic fluctuations, as in Gerolymos and Vallet [J. Fluid Mech. **851**, 447 (2018)] but simpler. The formula for each correlation has the same form. The accuracy of the model is validated in boundary layers where the intermodal correlation is weak.

DOI: 10.1103/PhysRevFluids.9.073401

I. INTRODUCTION

Shock wave/boundary layer interaction (SWBLI) is ubiquitous in aerodynamic and thermodynamic engineering applications. It usually has detrimental impacts on the performance of industrial designs, including efficiency loss, supersonic inlet surge, thermal and structural fatigue, and increased drag [1–3]. SWBLI induces abundant flow features, including unsteady shock motion, turbulence amplification and recovery, vortex shedding, flow separation and free shear layer, etc. [4–7]. After over 70 years of extensive research [8], it is still an active field. Take turbulence amplification as example, on which many experimental and numerical efforts have been made [9–13]. Pirozzoli and Grasso [10] conducted a direct numerical simulation (DNS) of incident SWBLI at Mach 2.25 to investigate the turbulence amplification process and the large-scale low-frequency unsteadiness. They ascribed the amplification to the formation of mixing layer. Likewise, Fang *et al.* [11] studied

*Contact author: wangjc@sustech.edu.cn
†Contact author: chensy@sustech.edu.cn

the mechanism of near-wall turbulence amplification by conducting a DNS at Mach 2.25. They showed that the amplification upstream is due to interaction of decelerated mean flow and fluctuating streamwise velocity, while the amplification downstream is induced by the shear layer. Yu *et al.* [12] studied the postshock turbulence recovery by conducting a DNS with similar flow conditions. They found that the amplification of turbulence induced by mixing layer and far-wall large-scale structures decay at different rates. Guo *et al.* [13] numerically investigated the amplification of turbulent kinetic energy and temperature fluctuations in a ramp-induced SWBLI at Mach 6. They found that the amplification can be attributed to the low-frequency unsteadiness and the free shear layer.

Despite the progress made by previous studies, several fundamental problems remain not satisfactorily resolved, which require a better understanding of the underlying physics of the flow features. One of such problems is to establish well-performed and physics-based models for Reynolds-averaged Navier-Stokes (RANS) simulation and large eddy simulation (LES) [14–16]. To improve the performance of RANS and LES, and to deepen the understanding of the interaction between different flow variables as well, there is urgent need to investigate the correlations between thermodynamic variables, as pointed out by many previous studies [17–21]. Gerolymos and Vallet [19] carried out DNSs of compressible turbulent channel flows at various Mach numbers to investigate the fluctuations of thermodynamic variables and discussed their scaling with Reynolds and Mach numbers. The correlations between the variables have been also systematically investigated. Their subsequent study [20] further discussed the range of validity of leading order approximations of the exact correlation formulas. Xu *et al.* [21] conducted DNSs of hypersonic turbulent boundary layer flows and thoroughly studied the correlation between thermodynamic variables by introducing Kovásznay decomposition. They decomposed the correlations into modal contributions. Adams [22] numerically investigated a ramp-induced SWBLI at Mach 3 and reported enhanced pressure-involved correlations in the shock-interaction region. However, to the best of our knowledge, systematic analyses on the correlations have never been conducted on SWBLI flows. Such analyses are of extraordinary importance, because as mentioned earlier, the intensities of turbulent and thermodynamic fluctuations are considerably enhanced in the shock-interaction region, which may have a profound impact on the correlations.

Apart from analyzing the contributing factors to the correlations, we also establish models for them for practical applications. The applicability of such models may be extended to various compressible thermodynamic turbulence in addition to SWBLI flows. As mentioned above, Gerolymos and Vallet [20] have developed the leading-order approximation model for the correlations. In their model, the correlations are deemed as functions of the root-mean-square (r.m.s.) values of thermodynamic fluctuations. This approach has many benefits. First, abundant observations and conclusions of r.m.s. values make those of correlations readily obtained. Second, combined with strong Reynolds analogy (SRA) theory or others, the correlations between thermodynamic variables can be extended to velocity-thermo correlations, which is meaningful for turbulence modeling. Third, it helps in fast prediction of correlations, without the bother of calculating second moment statistics. Last, the model may provide a different perspective to understand the nonlinear interaction between thermodynamic variables. Despite the advantages, the complexity of their formulas, especially of those related to entropy, hinders their application. Also, there are three inputs in their formulas, while the degree of freedom of thermodynamic r.m.s. values reduces to two if pressure and entropy are weakly correlated, as supposed by Kovásznay [23] and verified by many researchers [20,21]. The redundancy of inputs indicates a lesser important variable and not fully understood mechanism. It also suggests the possibility of simpler models.

One of the key control parameters in SWBLI is wall temperature, whose effect has been widely studied in supersonic and hypersonic wall-bounded flows [21,24–30]. The wall temperatures are typically lower than the recovery temperature, especially for high Mach numbers, due to considerable radiative cooling and internal heat transfer within the wall. However, it should be noted that under specific circumstances, a heated wall should instead be considered [3], whose effect on the flow properties may differ from a cooled wall in some respects. Bernardini *et al.* [25] carried out DNSs of SWBLI flows at Mach 2.28 with various isothermal wall conditions to investigate the

heat transfer and the effect of wall temperature. Two cooled-wall cases and two heated-wall cases, together with an adiabatic-wall case, were simulated. They observed that the interaction properties, including separation length, distribution of wall Stanton number and wall pressure fluctuations, etc., are greatly affected by wall temperature. A similar study conducted by Volpiani *et al.* [26] showed that wall temperature effect on the interaction region is mainly due to its effect on the incoming boundary layer. They also showed that wall cooling can be an effective means for flow control to reduce separation. Moreover, Xu *et al.* [21] showed that the correlations, at least those in the vicinity of the wall, are largely influenced by wall temperature. Therefore, it is of great importance to investigate wall temperature effect on the correlations in SWBLI flows.

The main objective of this study is to systematically investigate the second moment correlations between thermodynamic fluctuations in SWBLI flows. The concerned fluctuations are those of pressure, entropy, temperature, and density $\{p', s', T', \rho'\}$. The concerned correlations are $\{R_{p's'}, R_{p'T'}, R_{p'\rho'}, R_{s'T'}, R_{s'\rho'}, R_{T'\rho'}\}$. To achieve this objective, we propose an approach to quantify the contributing factors to the correlations and accordingly divide the flow fields into several zones to characterize their behaviors. Furthermore, we propose a simplified model to readily calculate the correlations using r.m.s. values of the fluctuations. The remainder of this paper is organized as follows. The governing equations and simulation parameters are listed in Sec. II. The results and analyses of the correlations are presented in Sec. III. The model for the correlations using r.m.s. values is derived and validated in Sec. IV. Finally, conclusions are given in Sec. V.

II. GOVERNING EQUATIONS AND SIMULATION PARAMETERS

The three-dimensional compressible Navier-Stokes equation can be nondimensionalized using free stream density ρ_∞, free stream velocity u_∞, reference length L_∞, free stream temperature T_∞, reference pressure $p_\infty = \rho_\infty u_\infty^2$, reference energy per unit volume $\rho_\infty u_\infty^2$, free stream viscosity μ_∞, and thermal conductivity κ_∞. Three dimensionless parameters are thus composed to govern the flow, namely, free stream Reynolds number $\mathrm{Re}_\infty = \rho_\infty u_\infty L_\infty/\mu_\infty$, free stream Mach number $\mathrm{Ma}_\infty = u_\infty/c_\infty$, and free stream Prandtl number $\mathrm{Pr}_\infty = \mu_\infty C_p/\kappa_\infty$, where $c_\infty = \sqrt{\gamma R T_\infty}$ is the free stream sound speed and C_p is the specific heat at constant pressure. γ, R, and C_p, together with C_v, specific heat at constant volume, are linked by relations $\gamma = C_p/C_v$ and $R = C_p - C_v$. Pr_∞ is assumed to be 0.7, while γ is assumed to be 1.4.

Correspondingly, the dimensionless Navier-Stokes equation in a Cartesian coordinate system can be written as [21,31]

$$\frac{\partial \rho}{\partial t} + \frac{\partial(\rho u_j)}{\partial x_j} = 0, \tag{1}$$

$$\frac{\partial(\rho u_i)}{\partial t} + \frac{\partial(\rho u_i u_j)}{\partial x_j} = -\frac{\partial p}{\partial x_i} + \frac{1}{\mathrm{Re}}\frac{\partial \sigma_{ij}}{\partial x_j}, \tag{2}$$

$$\frac{\partial E}{\partial t} + \frac{\partial[(E+p)u_j]}{\partial x_j} = -\frac{1}{\alpha}\frac{\partial}{\partial x_j}\left(\kappa\frac{\partial T}{\partial x_j}\right) + \frac{1}{\mathrm{Re}}\frac{\partial(\sigma_{ij}u_i)}{\partial x_j}, \tag{3}$$

$$p = \frac{\rho T}{\gamma \mathrm{Ma}_\infty^2}, \tag{4}$$

where ρ, u_i, p, E, and T are the dimensionless density, velocity, pressure, total energy per unit volume, and temperature, respectively. The parameter α is defined as $\alpha = (\gamma-1)\mathrm{Re}_\infty \mathrm{Pr}_\infty \mathrm{Ma}_\infty^2$. The viscous stress σ_{ij} is defined as $\sigma_{ij} = \mu(\frac{\partial u_i}{\partial x_j} + \frac{\partial u_j}{\partial x_i}) - \frac{2}{3}\mu\theta\delta_{ij}$, where $\theta = \frac{\partial u_k}{\partial x_k}$ is the velocity divergence and δ_{ij} is the Kronecker delta tensor. The dimensionless viscosity μ is calculated using Sutherland's law: $\mu = T^{3/2}[(1+S/T_\infty)/(T+110.4\mathrm{K}/T_\infty)]$. The dimensionless thermal conductivity κ is determined by the same formula as μ, assuming constant Pr and C_p. The total energy per unit volume E is defined as $E = \frac{p}{\gamma-1} + \frac{1}{2}\rho u_k u_k$.

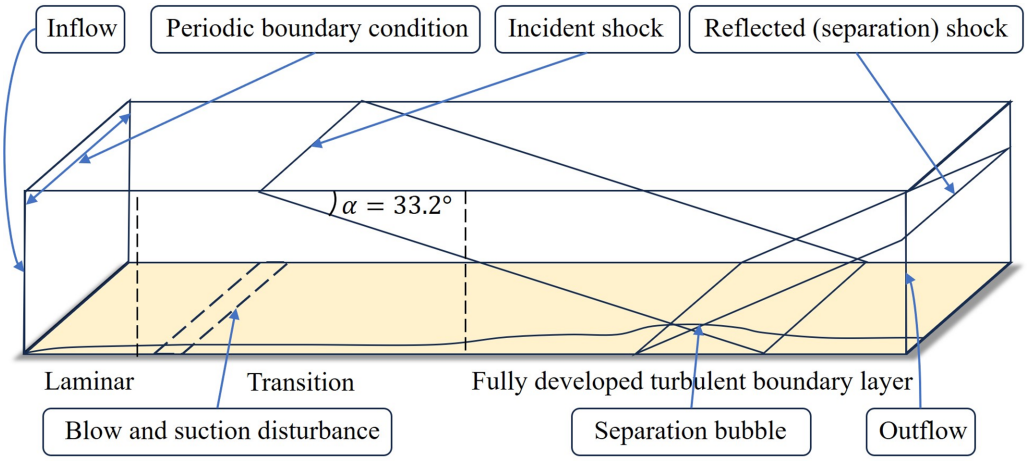

FIG. 1. A schematic of the flow.

The dimensionless equations (1)–(4) are directly solved using OpenCFD-SC code developed by Li *et al.* [32], which has been validated by many researchers in compressible flat plate boundary layer flows [21,33,34], compression ramp flows [35–37], and incident shock wave/boundary layer interaction flows [38–40]. The inviscid terms of the governing equations are discretized using a seventh-order weighted essentially nonoscillatory scheme [41], while the viscous terms are calculated by an eighth-order central differential scheme. A third-order total variation diminishing Runge-Kutta scheme is applied for time advancement. The simulation is conducted under the following boundary conditions: an inflow and an outflow condition, an upper far-field condition, a lower wall condition, and a spanwise periodic condition [38]. The schematic of the boundary conditions, along with the upstream boundary layer, the incident and reflected shock waves, the separation zone, and the reattached boundary layer, are shown in Fig. 1. The inflow condition is widely used in previous studies [11,38,42], where the free stream temperature $T_\infty = 169.44$ K and the free stream Mach number is $\mathrm{Ma}_\infty = 2.25$. According to Duan *et al.* [43], the wall recovery temperature T_r is defined as $T_r = T_\infty[1 + r(\gamma - 1)\mathrm{Ma}_\infty^2/2]$ with recovery factor $r = 0.9$. The wall-to-recovery temperature ratio S is further defined as $S = T_w/T_r$. To investigate the effect of wall temperature, three widely accepted isothermal wall conditions are selected: $S = 0.5, 1.0, 1.9$, labeled with "S05," "S10," and "S19," respectively [24–26,44]. A supplementary case with higher Reynolds number is conducted to expand the parameter space, labeled with "S10Re."

The fundamental computational parameters of the cases are listed in Table I, where the streamwise, wall normal, and spanwise directions are denoted by x, y, and z, respectively. Since the characteristics of the separation region are greatly affected by the upstream boundary layer [24,26], different free stream Reynolds numbers Re_∞ are selected to ensure comparative friction Reynolds numbers Re_τ in all the cases except case "S10Re."A nonslip velocity condition is applied at the lower wall boundary. Wall pressure is interpolated by inner points, and wall density is thus

TABLE I. Computational parameters.

Case	Re_∞	$L_x \times L_y \times L_z$	$N_x \times N_y \times N_z$	S	T_w/T_∞	x_{imp}	x_{ref}
S05	7800	137.7×25.0×4.4	3799×380×256	0.5	0.956	101.6	90.0
S10	25 200	137.7×25.0×4.4	3799×380×256	1.0	1.91	101.6	90.0
S19	66 000	137.7×25.0×4.4	3799×380×256	1.9	3.63	101.6	90.0
S10Re	32 000	240.1×18.0×6.2	5409×500×500	1.0	1.91	200.0	180.0

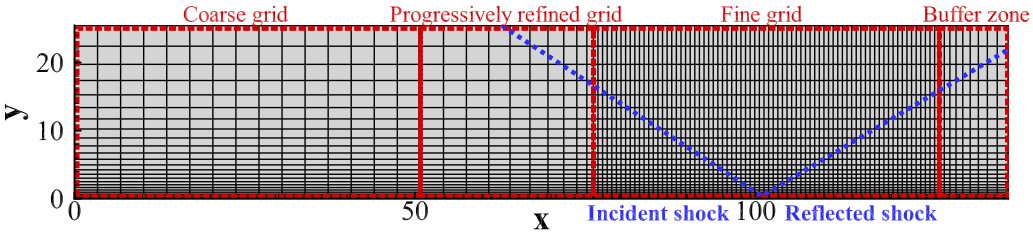

FIG. 2. Sketch of the computational meshes.

determined by Eq. (4). A nonreflecting condition is applied at the upper boundary and the outlet. The single-point Rankine-Hugoniot relations are applied at the upper boundary, so that an incident shock wave is induced at an angle $\alpha = 33.2^\circ$ to the main flow, with nominal shock impingement point at x_{imp}. The corresponding deflection angle (wedge angle) is $\varphi = 8.1^\circ$. At the outflow boundary, flow variables are interpolated by inner points.

The incoming flow generates a laminar boundary layer as it passes the wall. To induce laminar-to-turbulent transition, a wall-blowing-and-suction disturbance is implemented on the wall-normal velocity component v in a region between $x_a = 7.62$ and $x_b = 20.32$ [21,39]. Its detailed form can be found in Xu *et al.* [45]. After transition, the turbulent boundary layer continues to evolve for a distance and is impinged by the incident shock wave. The shock wave exerts a drastic adverse pressure gradient on the boundary layer, alters the turbulent structures, and for strong interaction, causes flow separation [46]. The strong shear on the separation bubble induces a shear layer. Downstream of the separation bubble is the reattachment region where the main flow is compressed by the shock waves. A sketch of the computational meshes for the first three cases is plotted in Fig. 2. Coarse grid is used for the boundary layer in laminar, transitional, and developing states, while fine meshes are applied for the fully developed boundary layer, the separation region, and the reattachment region [39,40]. Progressively refined resolution is applied between the two meshes. Moreover, a progressively coarse grid is implemented downstream of the fine meshes to avoid the reflection of disturbance caused by the numerical treatment at the outlet. Along the wall-normal direction, the grid spacing is exponentially increased, clustering about 192 nodes within the boundary layer. The spanwise grid is uniformly discretized. The meshes for the supplementary case are additionally refined. Validation of our database is presented in the Appendix.

To characterize the mean field and the turbulent fluctuations, Reynolds average (time and spanwise average) $\overline{f}$ and Favre average (density weighted average) $\tilde{f} = \overline{\rho f}/\overline{\rho}$ are introduced. The fluctuating components are $f' = f - \overline{f}$ and $f'' = f - \tilde{f}$, respectively. The averaged global characteristics are thus defined and listed in Table II. The viscous length scale δ_v is defined as $\delta_v = \overline{\mu}_w/\overline{\rho}_w u_\tau$, where subscript "$w$" denotes variables at the wall, $u_\tau = \sqrt{\tau_w/\overline{\rho}_w}$ is the friction velocity, and $\tau_w = (\frac{\partial \overline{u}}{\partial y})_{y=0}$ is the wall shear stress. Variables normalized using δ_v and u_τ are denoted with superscript "+." Furthermore, the semilocal scaling proposed by Huang *et al.* [47] is defined as $y^* = y/\delta_v^*$, where $\delta_v^* = \overline{\mu}/\overline{\rho} u_\tau^*$ and $u_\tau^* = \sqrt{\tau_w/\overline{\rho}}$. The boundary layer thickness δ is defined as the wall-normal distance between the wall and the location where the averaged streamwise velocity $\overline{u}$ attains $0.99u_\infty$. The displacement thickness and the momentum thickness can be written

TABLE II. Global characteristics at x_{ref}.

Case	δ	δ^*	θ	Re_τ	Re_θ	Re_{δ_2}	Δx^+	Δy_w^+	Δz^+
S05	1.57	0.311	0.145	547	1132	1179	5.9	0.44	6.0
S10	1.36	0.340	0.102	521	2580	1516	6.5	0.49	6.6
S19	1.32	0.402	0.0752	511	4966	1861	6.6	0.49	6.7
S10Re	2.96	0.650	0.247	1290	7904	2902	7.0	0.56	5.5

as [48] $\delta^* = \int_0^\delta (1 - \frac{\overline{\rho}\,\overline{u}}{\rho_\infty u_\infty})\,\mathrm{d}y$ and $\theta = \int_0^\delta \frac{\overline{\rho}\,\overline{u}}{\rho_\infty u_\infty}(1 - \frac{\overline{u}}{u_\infty})\,\mathrm{d}y$, respectively. Accordingly, the scaled interaction coordinate proposed by Volpiani *et al.* [26] is defined as $x_\delta = (x - x_{\mathrm{imp}})/\delta_{\mathrm{ref}}$.

The friction Reynolds number Re_τ is defined as $\mathrm{Re}_\tau = \overline{\rho}_w u_\tau \delta/\overline{\mu}_w$. It has been reported by Sillero *et al.* [49] that Re_τ can also be treated as $\delta^+ = \delta/\delta_v$ in the scaling of spatially developing turbulent boundary layers. The Reynolds number based on momentum thickness is defined as $\mathrm{Re}_\theta = \rho_\infty u_\infty \theta/\mu_\infty$, while the Reynolds number based on momentum thickness and wall viscosity can be written as $\mathrm{Re}_{\delta_2} = \rho_\infty u_\infty \theta/\mu_w$, which represents the ratio of the highest momentum to the wall shear stress. Also, the semilocal Reynolds number is defined as $\mathrm{Re}_\tau^* = \delta/(\delta_v^*)_e$, where subscript "*e*" denotes variables at the edge of the boundary layer [21]. The flow variables mentioned above are extracted at an upstream reference station x_{ref}, where the turbulent boundary layer is fully developed, and the downstream influence of SWBLI is negligible. Moreover, all the averages in our study are calculated using 270 instantaneous flow fields uniformly sampled in a time period of about $\Delta t = 290\delta_{\mathrm{ref}}/u_\infty$.

III. RESULTS AND ANALYSES OF THE CORRELATIONS

As mentioned in the introduction, Xu *et al.* [21] have decomposed the correlations into modal contributions by introducing Kovásznay decomposition. They have pointed out that the modal contributions are dependent on the relative intensity of the two modes. However, in their study, there is neither quantitative analysis on how the relative intensity affects the correlations, nor remarks on whether other factors could possibly influence the correlations.

In this section, we first show that there are only two parameters that determine the correlations, i.e., the intermodal competition $\Omega = s'_{\mathrm{rms}}/(p'_{\mathrm{rms}}/\overline{p})$ and the intermodal correlation $\Theta = R_{p's'}$. Then, according to modal intensities $p'_{\mathrm{rms}}/\overline{p}$ and s'_{rms}, we divide the flow fields of SWBLI into several zones with distinct physical properties to analyze the contributing factors to the correlations. After that, the spatial distributions of the two parameters Ω and Θ are displayed. Finally, the distributions of the other five correlations $\{R_{p'T'}, R_{p'\rho'}, R_{s'T'}, R_{s'\rho'}, R_{T'\rho'}\}$ are presented and discussed.

A. Derivation of the formulas

Our approach is based on Kovásznay decomposition [23,50], by which the fluctuations of thermodynamic variables can be decomposed into two modes, acoustic modes (denoted by subscript "*I*") and entropic modes (denoted by subscript "*E*"). The acoustic modes, linearly correlated with pressure fluctuations, are given by [31,51,52]

$$\begin{aligned} p'_I &= p - \overline{p}, \\ s'_I &= 0, \\ \rho'_I &= \frac{\overline{\rho} p'_I}{\gamma \overline{p}}, \\ T'_I &= \frac{(\gamma - 1)\overline{T} p'_I}{\gamma \overline{p}}. \end{aligned} \tag{5}$$

The entropic modes, which are supposed to be linearly (or at least strongly) correlated with entropy fluctuations, are defined as

$$\begin{aligned} p'_E &= 0, \\ s'_E &= s - \overline{s}, \\ \rho'_E &= \rho - \overline{\rho} - \rho'_I, \\ T'_E &= T - \overline{T} - T'_I, \end{aligned} \tag{6}$$

where the dimensionless entropy per unit mass s is defined as $s = \frac{1}{\gamma(\gamma-1)\mathrm{Ma}^2}\log(T/\rho^{\gamma-1})$ [19,31]. Using DNS data, the supposed linear correlations between s' and the entropic modes are verified in the entire boundary layer (including the shock-interaction region) with magnitudes of $R_{s'T'_E}$ and $R_{s'\rho'_E}$ higher than 0.99 (not shown for brevity), consistent with previous studies [21]. Alternatively, the entropic modes of density and temperature can be defined as $\rho'_E = -(\gamma-1)\mathrm{Ma}^2 s'_E$ and $T'_E = (\gamma-1)\mathrm{Ma}^2 s'_E$. This definition ensures the linear correlation but results in residue, so hereinafter we adopt Eq. (6) to avoid the residue unless otherwise stated. This alternative definition is used only to explicitly express the coefficients.

The correlation coefficient between two fluctuating thermodynamic variables ϕ' and ψ' is given by

$$R_{\phi'\psi'} = \frac{\overline{\phi'\psi'}}{\sqrt{\overline{\phi'^2}}\sqrt{\overline{\psi'^2}}}. \tag{7}$$

Applying Kovásznay decomposition, the correlation coefficient can be written as

$$R_{\phi'\psi'} = \frac{\overline{(\phi'_I+\phi'_E)(\psi'_I+\psi'_E)}}{\sqrt{\overline{\phi'^2}}\sqrt{\overline{\psi'^2}}} = M_{\phi'_I\psi'_I} + M_{\phi'_I\psi'_E} + M_{\phi'_E\psi'_I} + M_{\phi'_E\psi'_E}, \tag{8}$$

where $M_{\phi'_I\psi'_I} = \frac{\overline{\phi'_I\psi'_I}}{\sqrt{\overline{\phi'^2}}\sqrt{\overline{\psi'^2}}}$ and other three terms are the modal contributions, as in Xu *et al.* [21]. Take $M_{\phi'_I\psi'_I}$ as an example; it can be further written as

$$M_{\phi'_I\psi'_I} = \frac{\overline{\phi'_I\psi'_I}}{\sqrt{\overline{\phi'^2_I}}\sqrt{\overline{\psi'^2_I}}}\frac{\sqrt{\overline{\phi'^2_I}}}{\sqrt{\overline{\phi'^2}}}\frac{\sqrt{\overline{\psi'^2_I}}}{\sqrt{\overline{\psi'^2}}} \equiv R_{\phi'_I\psi'_I} I_{\phi I} I_{\psi I}, \tag{9}$$

where $R_{\phi'_I\psi'_I} = \frac{\overline{\phi'_I\psi'_I}}{\sqrt{\overline{\phi'^2_I}}\sqrt{\overline{\psi'^2_I}}}$ is the correlation coefficient between ϕ'_I and ψ'_I, and $I_{\phi I} \equiv \frac{\sqrt{\overline{\phi'^2_I}}}{\sqrt{\overline{\phi'^2}}}$ is the ratio of modal r.m.s. to total r.m.s.

For convenience, write the intermodal correlation $R_{p's'} \equiv \Theta$ and let ρ' appear only at the position of ψ'. Assume the entropic modes of density and temperature are linearly correlated with fluctuating entropy [21], $R_{s'\rho'_E} = -1$ and $R_{s'T'_E} = 1$, then Eq. (8) can be rewritten as

$$R_{\phi'\psi'} = I_{\phi I} I_{\psi I} \pm \Theta I_{\phi I} I_{\psi E} + \Theta I_{\phi E} I_{\psi I} \pm I_{\phi E} I_{\psi E}, \tag{10}$$

where the plus-minus sign takes negative if ψ' is ρ'. Here $R_{\phi'\psi'}$ can be seen as a function of the r.m.s. values and Θ. A defect of this formula is that there are too many input variables. From Eqs. (5) and (6) we know $I_{pI} = 1$, $I_{pE} = 0$, $I_{sI} = 0$, and $I_{sE} = 1$. Thus, Eq. (10) can be simplified and specified as

$$\begin{aligned}
R_{p's'} &= \Theta, \\
R_{p'T'} &= I_{TI} + \Theta I_{\mathrm{TE}}, \\
R_{p'\rho'} &= I_{\rho I} - \Theta I_{\rho E}, \\
R_{s'T'} &= \Theta I_{TI} + I_{\mathrm{TE}}, \\
R_{s'\rho'} &= \Theta I_{\rho I} - I_{\rho E}, \\
R_{T'\rho'} &= I_{TI} I_{\rho I} - \Theta I_{TI} I_{\rho E} + \Theta I_{\mathrm{TE}} I_{\rho I} - I_{\mathrm{TE}} I_{\rho E}.
\end{aligned} \tag{11}$$

Applying Kovásznay decomposition again, the r.m.s. values of density and temperature satisfies

$$\begin{aligned}
\rho'^2_{\mathrm{rms}} &= \rho'^2_{\mathrm{Irms}} + \rho'^2_{\mathrm{Erms}} - 2\Theta\rho'_{\mathrm{Irms}}\rho'_{\mathrm{Erms}}, \\
T'^2_{\mathrm{rms}} &= T'^2_{\mathrm{Irms}} + T'^2_{\mathrm{Erms}} + 2\Theta T'_{\mathrm{Irms}} T'_{\mathrm{Erms}}.
\end{aligned} \tag{12}$$

Therefore, the four r.m.s. ratios which appear in Eq. (11) can be further written as

$$
\begin{aligned}
I_{\rho I}(\Omega, \Theta) &= [1 - \Theta^2 + (k_\rho \Omega - 2\Theta)^2]^{-1/2}, \\
I_{\rho E}(\Omega, \Theta) &= [1 - \Theta^2 + (1/k_\rho \Omega - 2\Theta)^2]^{-1/2}, \\
I_{\mathrm{TI}}(\Omega, \Theta) &= [1 - \Theta^2 + (k_T \Omega + 2\Theta)^2]^{-1/2}, \\
I_{\mathrm{TE}}(\Omega, \Theta) &= [1 - \Theta^2 + (1/k_T \Omega + 2\Theta)^2]^{-1/2},
\end{aligned} \tag{13}
$$

where $\Omega \equiv s'_{\mathrm{rms}}/(p'_{\mathrm{rms}}/\overline{p})$ represents the intermodal competition, and $k_\rho = (\rho'_{\mathrm{Erms}}/\rho'_{\mathrm{Irms}})/\Omega$ and $k_T = (T'_{\mathrm{Erms}}/T'_{\mathrm{Irms}})/\Omega$ are coefficients dependent on γ and Ma. If we apply the alternative definition of entropic modes mentioned above (just in order to express the coefficients explicitly), then $k_\rho = \gamma(\gamma - 1)\mathrm{Ma}^2$ and $k_T = \gamma \mathrm{Ma}^2$. It can be seen that the r.m.s. ratios, and thus the correlations, are functions of merely Ω and Θ, while the magnitudes of the r.m.s. values have no direct influence on the correlations. Also the input variables are the same for different correlations. In the remainder of this section, we apply Eqs. (11) and (13) to analyze the influence of Ω and Θ in different zones of the flow on the concerned correlations.

B. Division of the flow

According to Eqs. (11) and (13), the concerned correlations are functions of Ω and Θ, the former of which is the ratio of $p'_{\mathrm{rms}}/\overline{p}$ to s'_{rms}. Therefore, to investigate the underlying mechanism of the correlations, there is need to analyze first the spatial distributions of these two r.m.s. values. In this subsection, we try to divide the flow fields of SWBLI into several zones with distinct physical properties. Such a division helps in determining the major flow feature that results in the correlations. The profiles of normalized r.m.s. values of pressure fluctuations $p'_{\mathrm{rms}}/\overline{p}$ and r.m.s. values of entropy fluctuations s'_{rms} in inner scaling are plotted in Fig. 3. Two streamwise locations, $x = x_{\mathrm{ref}}$ and $x = x_{\mathrm{imp}}$, are selected to characterize the flow in the upstream boundary layer and in the shock-interaction region. It can be seen that in the upstream boundary layer, consistent with previous studies [21], $p'_{\mathrm{rms}}/\overline{p}$ is intense near the wall and weakens as wall distance increases. In contrast, in the interaction region, the peak value of $p'_{\mathrm{rms}}/\overline{p}$ drifts away from the wall, which indicates the presence and influence of free shear layer [11]. Note that $p'_{\mathrm{rms}}/\overline{p}$ is largely intensified in the interaction region. Cases with distinct wall temperatures are merely quantitatively different. The higher the wall temperature, the weaker the fluctuation intensity. Reynolds number has a minor effect on $p'_{\mathrm{rms}}/\overline{p}$.

The distributions of s'_{rms} are more complex. In the upstream boundary layer, consistent with previous studies [21], s'_{rms} is quite weak in the viscous sublayer in all cases. This can be attributed to the hindrance of the strong viscosity exerted by the wall to turbulent heat transfer. Note that the thickness of this layer is merely several viscous length units. In the adiabatic and wall-heating cases, upon this layer is a buffer layer (at about $y^* = 10$), followed by a layer with intense s'_{rms}, the formation of which can be attributed to high turbulent heat transfer. In the wall-cooling case, however, there is no space for the buffer layer. From the profiles of wall-normal gradient of mean temperature $\partial\overline{T}/\partial y$ and r.m.s. of wall-normal velocity fluctuations v'_{rms} (not shown for brevity) it can be seen that the high s'_{rms} layer is where the levels of both $\partial\overline{T}/\partial y$ and v'_{rms} are high, which indicates that the intense s'_{rms} results from turbulent heat transfer. It should be noted that the high s'_{rms} layer in case "S05" is separated into two by a layer where s'_{rms} is relatively low. This can be attributed to the fact that there is an inflection point (at about $y^* = 20$) in the temperature profile in the wall-cooling case, where $\partial\overline{T}/\partial y = 0$.

In the interaction region, similarly, the distribution of s'_{rms} in case "S05" is also different from those in other cases. It can be seen later in Fig. 4 that the flow separation in case "S05" is much weaker than in other cases, which results in the difference in s'_{rms}. In case "S05," due to weak flow separation, the trend of s'_{rms} is not substantially different from that upstream. The near-wall high s'_{rms} layer is thickened and augmented to a large extent but still attached to the wall, and the

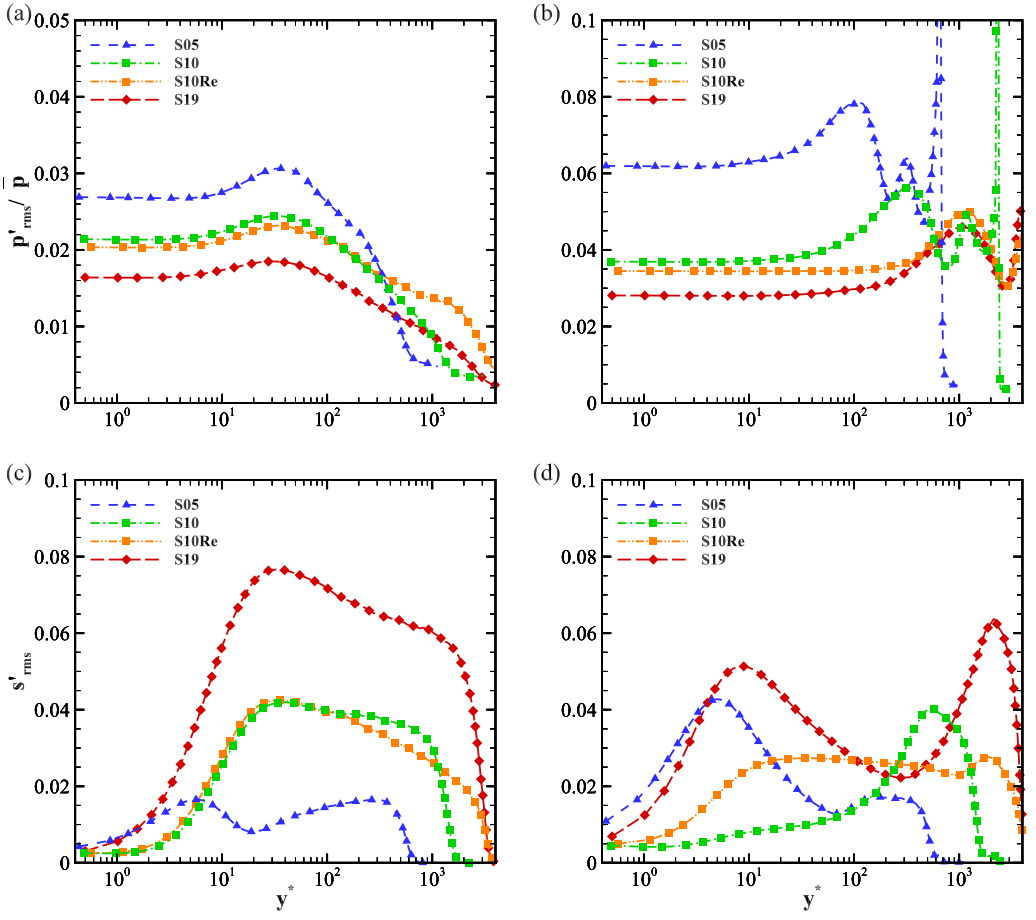

FIG. 3. Profiles of (a), (b) $p'_{\rm rms}/\overline{p}$ and (c), (d) $s'_{\rm rms}$. (a), (c), In the upstream boundary layer $x = x_{\rm ref}$; (b), (d), in the shock-interaction region $x = x_{\rm imp}$.

low $s'_{\rm rms}$ layer upon it is slightly elevated. The bottom low $s'_{\rm rms}$ layer and the outer high $s'_{\rm rms}$ layer remain almost unaffected. Note that the outer high $s'_{\rm rms}$ layer is weaker than the inner one due to weak separation. In the adiabatic and wall-heating cases, the separation bubbles are obvious and the strong $s'_{\rm rms}$ layers are highly elevated (see Fig. 4). In the separation bubble, the temperature gradient $\partial\overline{T}/\partial y$ is relatively small, which results in substantially thickened wall-attached low $s'_{\rm rms}$ layer. The main difference in the wall-heating case is that the buffer layer is remained in the separation bubble due to larger temperature gradient. The Reynolds number effect on $s'_{\rm rms}$ is mainly reflected in the separation bubble, where $s'_{\rm rms}$ is weak in case "S10" but strong in case "S10Re" (see Fig. 4). This may be ascribed to the fact that the shocks can reach closer to the wall in case "S10Re."

The distributions of $p'_{\rm rms}/\overline{p}$ in xy plane in outer scaling are depicted in Fig. 5. As can be seen, the intensity of pressure fluctuations are strong near the incident and reflected shocks, which can be ascribed to the unsteady shock motion [11]. Strong compression and dilatation are also observed near the tip of the incident shock, the deflection point of the shear layer, and the expansion fan. Inside the boundary layer, the peak of $p'_{\rm rms}/\overline{p}$ coincides with that of the turbulent Mach number and that of the mean shear (not shown), which indicates that the high $p'_{\rm rms}$ is caused by the free shear layer [11]. As the shear layer dissipates downstream, $p'_{\rm rms}/\overline{p}$ also weakens. As wall temperature increases, the streamwise length of interaction region is increased. Increasing Reynolds number results in

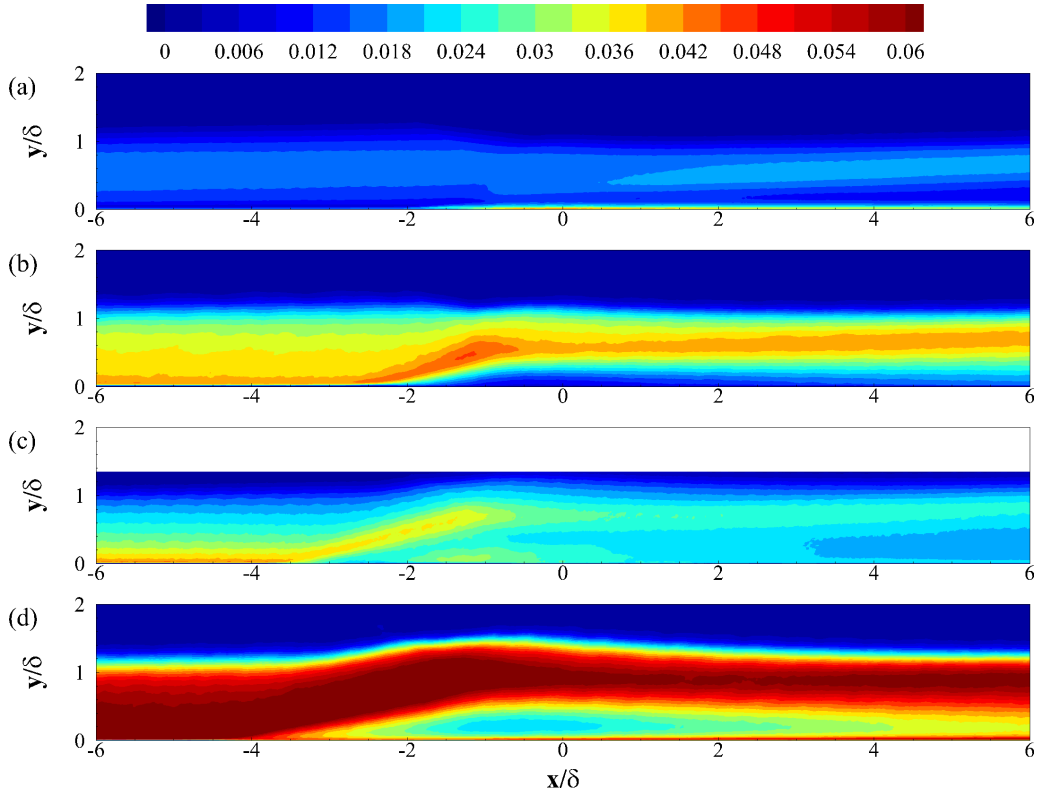

FIG. 4. Distributions of $s'_{\rm rms}$ in xy plane in outer scaling. (a) Case "S05"; (b) case "S10"; (c) case "S10Re"; (d) case "S19".

a similar phenomenon. In specifics, the reflected shock foot and the onset of free shear layer reach farther upstream. Also, as wall temperature increases, the peak values of $p'_{\rm rms}/\overline{p}$ in both the upstream boundary layer and the free shear layer are weakened. Note that the presence of flow separation seems to have little influence on the distributions of $p'_{\rm rms}/\overline{p}$. The distributions of $s'_{\rm rms}$ in the xy plane in outer scaling are illustrated in Fig. 4. The above analyses of $s'_{\rm rms}$ are confirmed. It is observed that the peak value of $s'_{\rm rms}$ is farther from the wall than that of $p'_{\rm rms}/\overline{p}$ (the core of free shear layer). It should also be noted that the temperature of the cooled wall is close to the free stream temperature ($T_w = 0.956T_\infty$), and as a result, the temperature gradient is stronger as wall temperature increases. This further results in stronger entropic modes in cases with higher wall temperatures.

We have displayed above the distributions of $p'_{\rm rms}/\overline{p}$ and $s'_{\rm rms}$. The distributions of other two normalized r.m.s. values, i.e., that of density $\rho'_{\rm rms}/\overline{\rho}$ and that of temperature $T'_{\rm rms}/\overline{T}$, are omitted for brevity. The omission is because $\rho'_{\rm rms}/\overline{\rho}$ and $T'_{\rm rms}/\overline{T}$ are dependent variables, which are determined, at least in regions where $R_{p's'}$ is weak, by $p'_{\rm rms}/\overline{p}$ and $s'_{\rm rms}$, according to Eq. (12).

It can be concluded that, in terms of the distributions of $p'_{\rm rms}/\overline{p}$ and $s'_{\rm rms}$, the flow field in the wall-cooling case without separation can be divided into (I) a near-wall viscous sublayer where $p'_{\rm rms}/\overline{p}$ is strong but $s'_{\rm rms}$ is relatively weak, (II) an inner high $s'_{\rm rms}$ layer, which is thickened and augmented in the interaction region, (III) a relatively low $s'_{\rm rms}$ layer where $p'_{\rm rms}/\overline{p}$ attains its peak and starts to decline, (IV) an outer high $s'_{\rm rms}$ layer where $p'_{\rm rms}/\overline{p}$ is weak, (V) a (not much elevated) free shear layer where $p'_{\rm rms}/\overline{p}$ attains its peak, and (VI) an area around the shocks and the expansion fan where $p'_{\rm rms}/\overline{p}$ is intense. The upstream layers are not much affected in the shock-interaction region. In contrast, flow fields in the adiabatic and the wall-heating cases with remarkable separation can be divided into (I) a similar near-wall viscous sublayer, (II) a buffer layer where $s'_{\rm rms}$ increases rapidly,

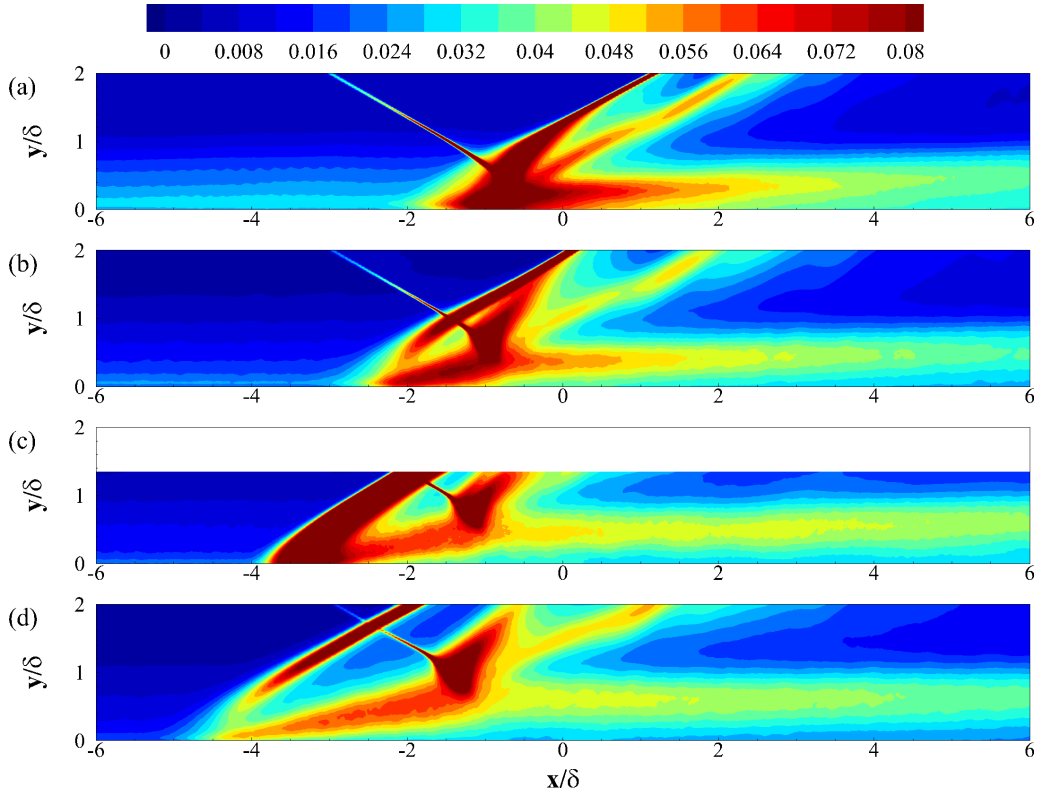

FIG. 5. Distributions of $p'_{\mathrm{rms}}/\overline{p}$ in xy plane in outer scaling. (a) case "S05"; (b) case "S10"; (c) case "S10Re"; (d) case "S19".

(III) a thick layer with declining $p'_{\mathrm{rms}}/\overline{p}$ but high s'_{rms}, (IV) the separation bubble and its downstream areas where $p'_{\mathrm{rms}}/\overline{p}$ is strong but s'_{rms} is weak, (V) the (much elevated) free shear layer with peak $p'_{\mathrm{rms}}/\overline{p}$, (VI) the even higher elevated strong s'_{rms} layer, and (VII) area around the shocks and the expansion fan.

C. Intermodal competition and intermodal correlation

As mentioned above, the two factors that function in the r.m.s. ratios, and thus in the correlations, are the intermodal competition Ω and the intermodal correlation Θ. Analyses based on Ω and Θ are clearer than those based on the four r.m.s. values, due to less and uniform input variables. Hence, the distributions of $\log\Omega$ and Θ are illustrated in this subsection. The reason for taking logarithm is because Ω is the ratio of the intensities of two modes and should not be biased towards any one. Negative $\log\Omega$ represents the dominance of acoustic modes, while positive $\log\Omega$ indicates that of entropic modes.

The distributions of $\log\Omega$ in inner and outer scalings are plotted in Fig. 6. It can be seen that the effect of wall temperature is remarkable. In the upstream boundary layers, due to the uniform distribution of $p'_{\mathrm{rms}}/\overline{p}$ near the wall, the profile of $\log\Omega$ near the wall is basically that of s'_{rms} [see Figs. 3(a) and 3(c) and 6(a)]. In the far-wall region, $\log\Omega$ is much increased due to the decline of $p'_{\mathrm{rms}}/\overline{p}$ and the enhancement of s'_{rms}. In the interaction region, the wall-normal distributions of $\log\Omega$ are also different with different wall temperatures. The dominance of entropic modes is more prominent as wall temperature increases. In case "S05," almost the entire flow field is dominated by acoustic modes, while in case "S19," it is the other way around. In all the cases, acoustic modes

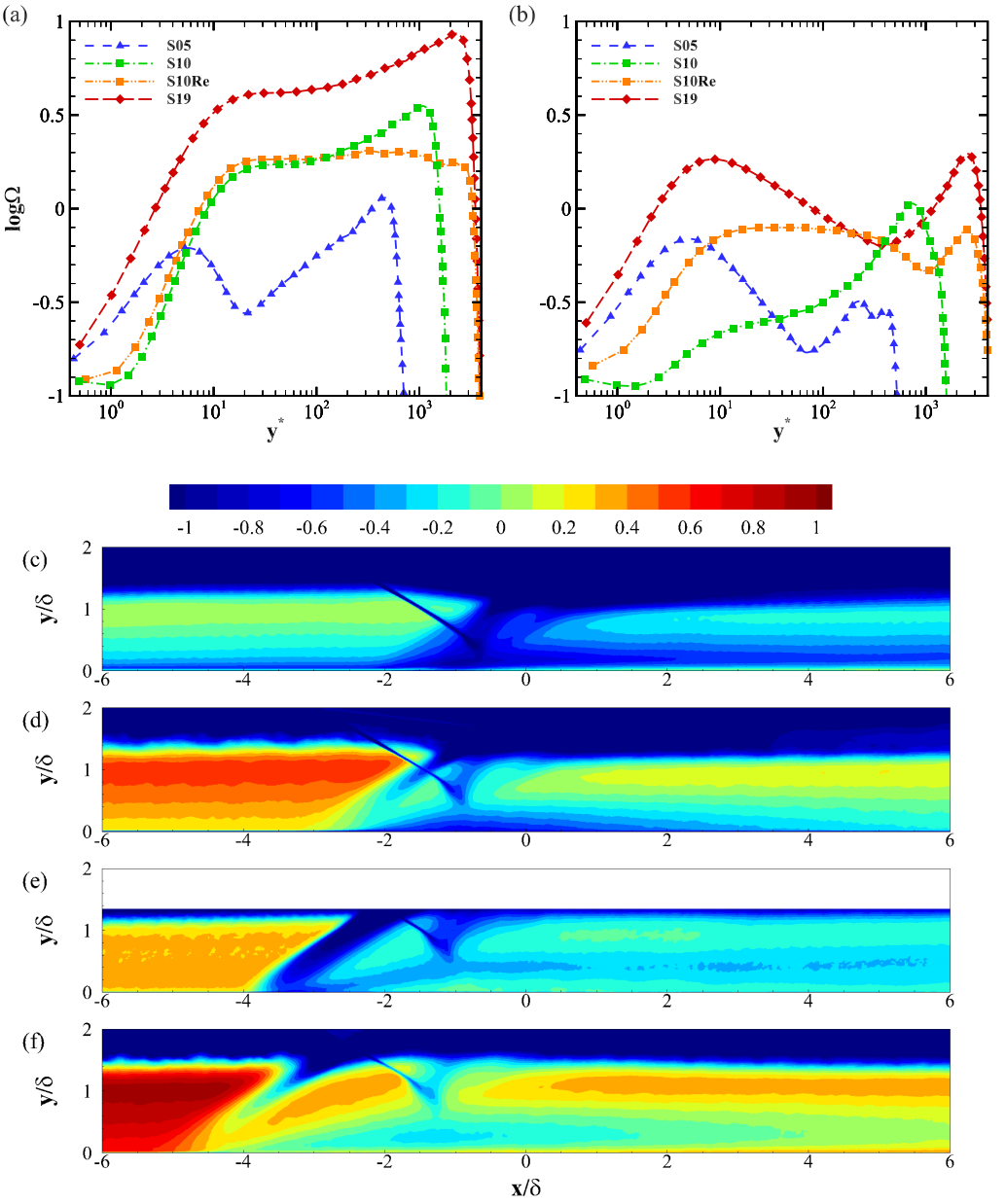

FIG. 6. Distributions of logΩ in (a), (b) inner scaling and (c)–(f) outer scaling. (a) In the upstream boundary layer $x = x_{\mathrm{ref}}$; (b) in the shock-interaction region $x = x_{\mathrm{imp}}$; (c) case "S05"; (d) case "S10"; (e) case "S10Re"; (f) case "S19".

predominate in the viscous sublayer. In case "S05," it is followed by the attached inner high s'_{rms} layer where the intensity of the two modes is comparable. Above it are the low-temperature gradient layer and the "not much elevated" free shear layer, where acoustic modes predominate. On top of them is the outer high s'_{rms} layer, where the entropic modes are slightly stronger than below but still weaker than acoustic modes. In cases with higher wall temperatures, the separation bubbles are larger, in which the acoustic modes are in the ascendancy. It is interesting to notice that in

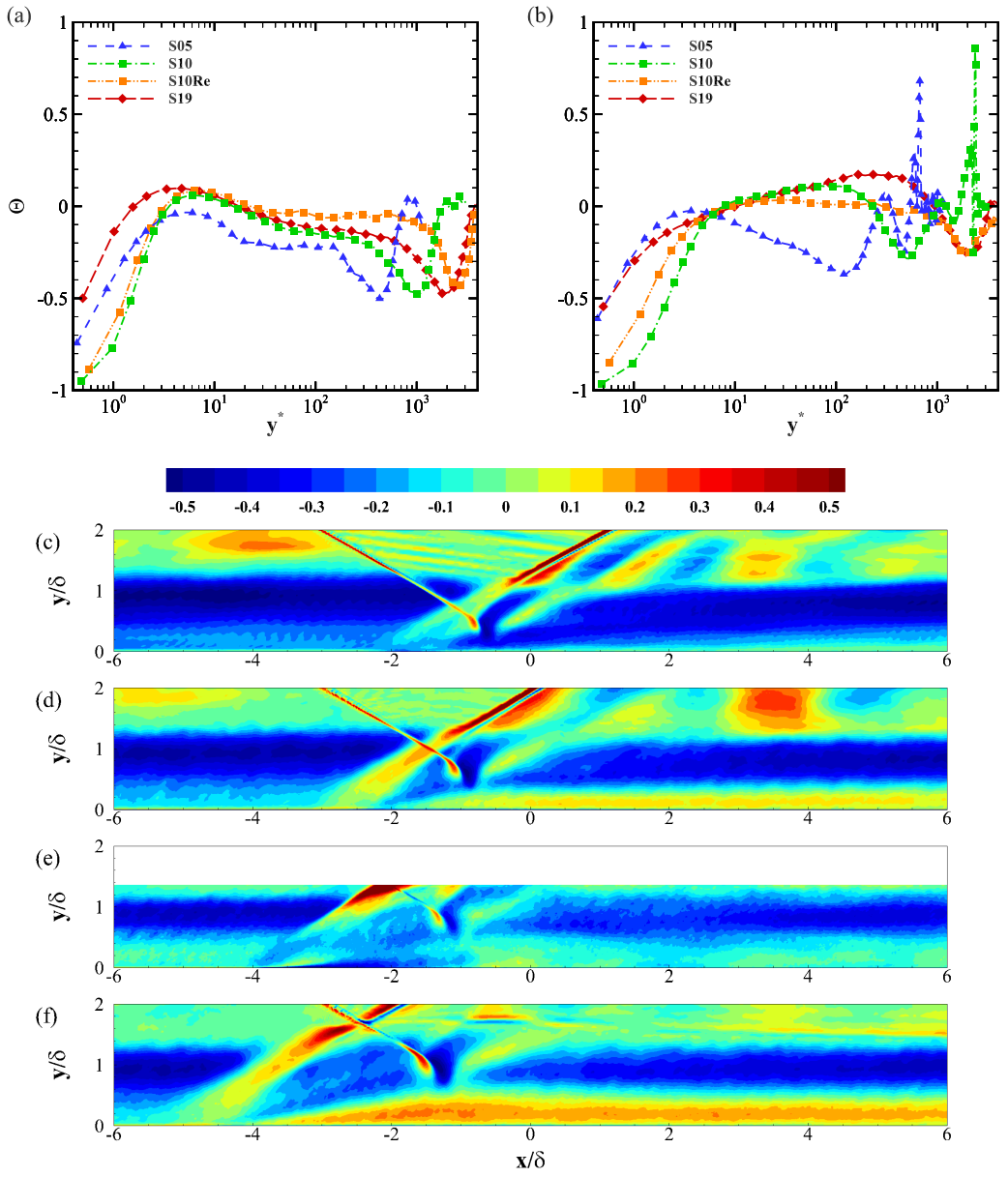

FIG. 7. Distributions of Θ in (a), (b) inner scaling and (c)–(f) outer scaling. (a) In the upstream boundary layer $x = x_{\mathrm{ref}}$; (b) in the shock-interaction region $x = x_{\mathrm{imp}}$; (c) case "S05"; (d) case "S10"; (e) case "S10Re"; (f) case "S19".

these cases, weak Ω does not appear in regions where $p'_{\mathrm{rms}}/\overline{p}$ is the strongest but where s'_{rms} is the weakest. As mentioned above, the profile in the wall-heating case differs with those in adiabatic cases by a near-wall entropy-dominating layer. This layer is also vaguely observed in case "S10Re". Therefore, the effect of increasing Reynolds number is to some extent similar to that of increasing wall temperature.

The distributions of Θ in inner and outer scalings are shown in Fig. 7. Note that the correlations outside the boundary layer caused by the intermittent behavior of the turbulent/nonturbulent

interface (TNTI) [21] are not addressed in our study. It can bee seen that large values of Θ mainly appear in the vicinity of the wall and near the edge of the boundary layer, which is consistent with previous studies [21]. Near the edge of the boundary layer, the correlation is strenthened to around -0.5. In the shock-interaction region, there is only a small area near the tip of the incident shock, the deflection point of the shear layer, and the expansion fan where Θ is also slightly strong (this is also where $p'_{\rm rms}/\overline{p}$ is intense, as mentioned earlier). It should also be noted that $R_{p's'}$ tends to -1 at the wall due to strictly isothermal wall condition (since $T' = T'_I + T'_E = 0$, $T'_I = -T'_E$). Other conclusions with isothermal wall condition include $R_{p'\rho'} = 1$ and $R_{s'\rho'} = -1$ (see Figs. 10 and 12 below) [19]. The affected area is limited to $y^* < 2$ in the upstream boundary layers, but the layer may be thickened by several viscous units in the interaction region. As wall distance increases, Θ recovers rapidly from -1 at the wall to about -0.2 outside the viscous sublayer. In the separation bubble and near the shocks, Θ can be weakly positive. In most regions of the flow, p' and s' are weakly negatively correlated. Wall temperature and Reynolds number have minor impacts on the distributions of Θ. Their effects are mainly on the streamwise interaction length, the presence of separation bubble, and the weak Θ inside the bubble.

D. Other five correlations

To visually present the effects of Ω and Θ, maps for the correlations in Ω-Θ space are illustrated in Fig. 8, according to Eqs. (11) and (13). Ω is plotted in logarithmic scale and only results in $0.1 \leqslant \Omega \leqslant 10$ are shown. In this subsection, we draw conclusions according to the maps with Ω and Θ varying in this selected range. It should be noted that it is unlikely for every point in Ω-Θ space to appear in experiments and simulations. For example, strongly positive Θ is not detected in our databases. The map for $R_{p's'}$ is omitted since $R_{p's'} = \Theta$. The distributions of the other five correlations in inner and outer scalings are depicted in Figs. 9–13, respectively. In different zones of the flow fields identified earlier, (Ω, Θ) varies to a large extent. Therefore, the spatial distributions of the correlations serve as excellent benchmarks to examine the correctness of the conclusions drawn from the maps.

It can be seen that the maps for $R_{p'T'}$ and $R_{p'\rho'}$ are similar to each other, with one turned upside down. In most areas of Ω-Θ space, $R_{p'T'}$ increases as Ω decreases and as Θ increases, while $R_{p'\rho'}$ increases as Ω decreases and as Θ decreases. Note that in most regions of the flow, the two modes are weakly negatively correlated. Therefore, $R_{p'T'}$ is supposed to be weak [see Fig. 9(a)] unless acoustic modes are overwhelmingly stronger than entropic modes [see area near the reflected shock in Fig. 9(c)]. A similar conclusion can be drawn for $R_{p'\rho'}$, with the difference that acoustic modes do not have to be that dominant to yield strong $R_{p'\rho'}$ (see Figs. 9 and 10 where $R_{p'\rho'}$ is generally stronger than $R_{p'T'}$). The observation that acoustic modes have larger influence on density than temperature is consistent with previous studies [21,31].

As mentioned above, Θ is also possible to be strongly negative, in the vicinity of the wall or near the edge of the boundary layer. In such regions, $R_{p'\rho'}$ is supposed to be strongly positive, regardless of Ω [see Fig. 10(a)]. In contrast, $R_{p'T'}$ is largely dependent on Ω. In the near-wall case, due to the strictly isothermo wall condition, the value of Ω is not arbitrary as Θ tends to -1. Applying the alternative definition of entropic modes yields $\log\Omega = \log(1/\gamma {\rm Ma}^2) \approx -0.85$ [see Figs. 6(a) and 6(b)]. It is interesting to notice that $(\log\Omega, \Theta) = (-0.85, -1)$ is exactly a singular point where $k_T\Omega = 1$ and thus $R_{p'T'} = 0$. Therefore, $R_{p'T'}$ in this extremely thin layer is supposed to be highly sensitive to Ω and Θ and disparate in different cases [see Figs. 9(a) and 9(b) where the correlations in viscous sublayer in different cases are diverse]. Such a singular point also exists in the map for $R_{p'\rho'}$, where $k_\rho\Omega = 1$ and $\Theta = 1$, but as mentioned above, Θ is unlikely to be strongly positive in our databases. Near the edge of the boundary layer, due to the dominance of entropic modes, $R_{p'T'}$ is supposed to be strongly negative [see Figs. 9(c)–9(f)]. The chances are that Θ will be weakly positive, for instance, in the separation bubble and near the shocks. $R_{p'T'}$ is slightly strengthened there, while $R_{p'\rho'}$ is slightly weakened [see the separation bubbles in Figs. 9(f) and 10(f)].

The maps for $R_{s'T'}$ and $R_{s'\rho'}$ are also similar to each other, with one turned upside down. It can be seen that in the selected range of Ω, $R_{s'T'}$ is most likely to be strongly positive (see Fig. 11), and

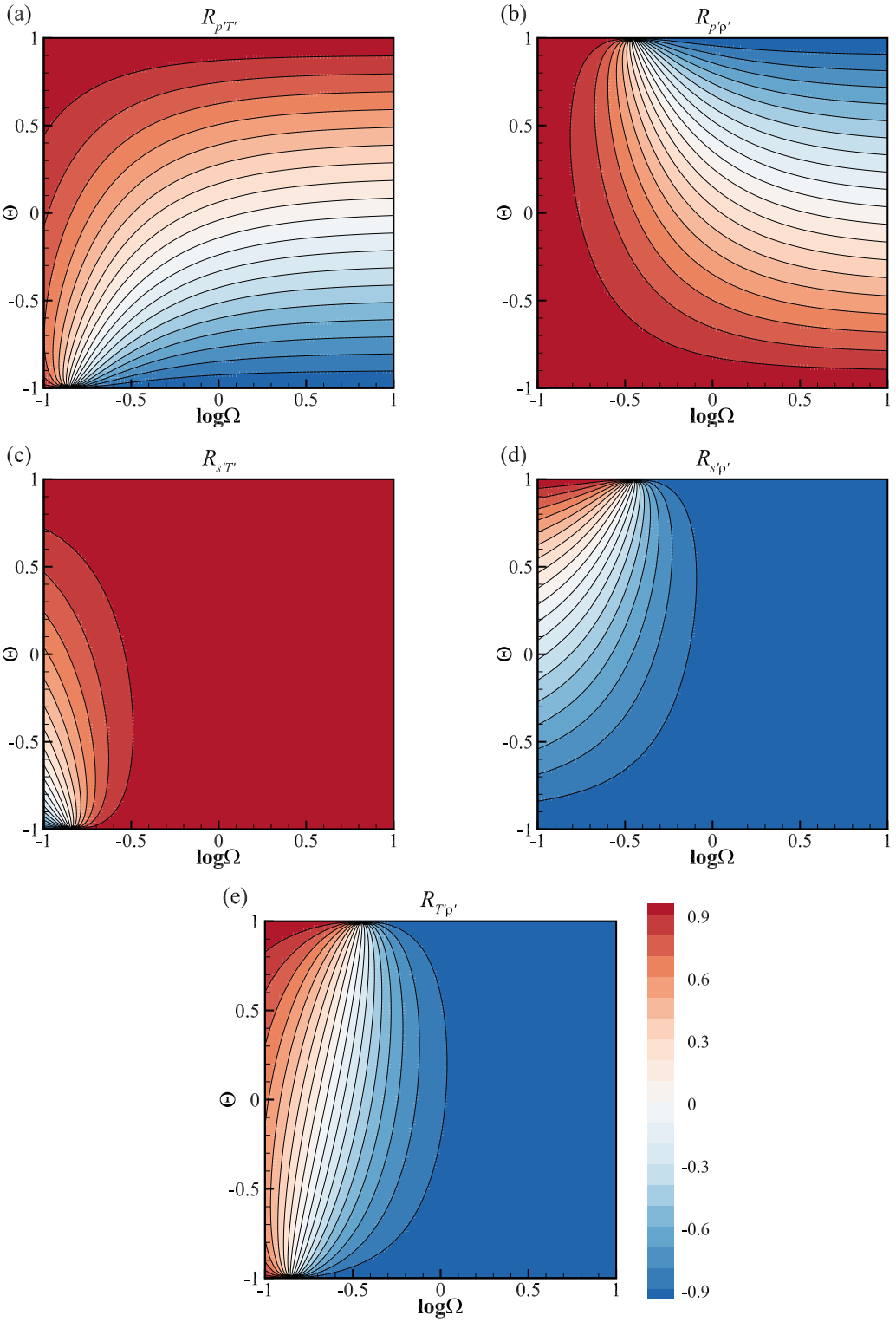

FIG. 8. Maps for the correlations in Ω-Θ space.

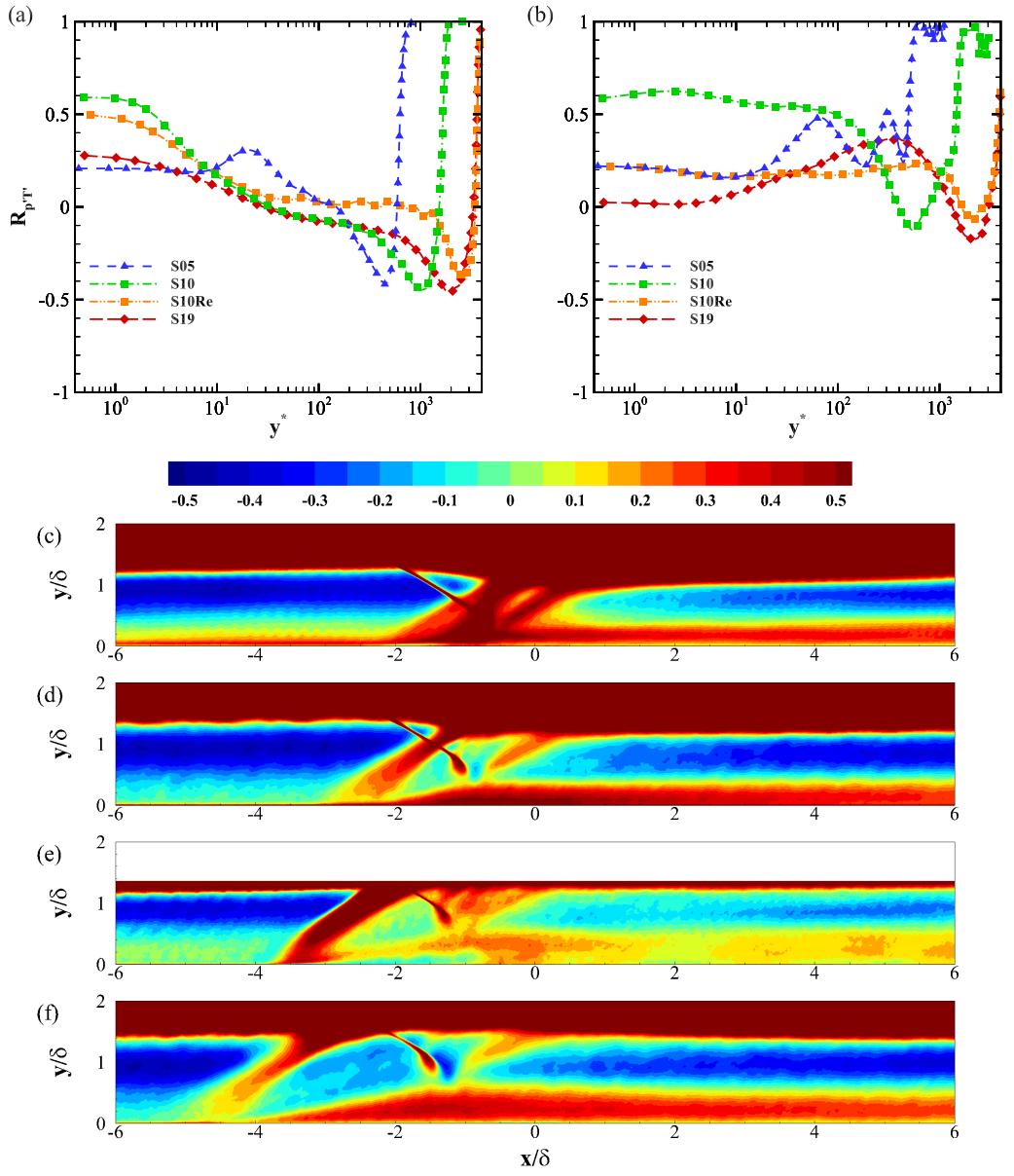

FIG. 9. Distributions of $R_{p'T'}$ in (a), (b) inner scaling and (c)–(f) outer scaling. (a) In the upstream boundary layer $x = x_{\text{ref}}$; (b) in the shock-interaction region $x = x_{\text{imp}}$; (c) case "S05"; (d) case "S10"; (e) case "S10Re"; (f) case "S19".

$R_{s'\rho'}$ strongly negative (see Fig. 12). The map for $R_{s'T'}$ is more extreme, where weak and negative correlations appear only when both $\log\Omega$ and Θ tend to -1 [see the viscous sublayer in Fig. 11(a)]. In most regions of the flow where Θ is weakly negative, it is hard to change the signs of $R_{s'T'}$ and $R_{s'\rho'}$ even when acoustic modes are quite strong [see Figs. 11(a) and 11(b) and 12(a) and 12(b)].

It should be noted that $R_{s'T'} = -R_{p'T'}$ and $R_{s'\rho'} = -R_{p'\rho'}$ when $\Theta = -1$. Therefore, in the regions with strongly negative Θ mentioned above, $R_{s'\rho'}$ is strongly negative, regardless of Ω [see Fig. 12(a)]. For $R_{s'T'}$, the singular point $(\log\Omega, \Theta) = (-0.85, -1)$ is also where the correlation is

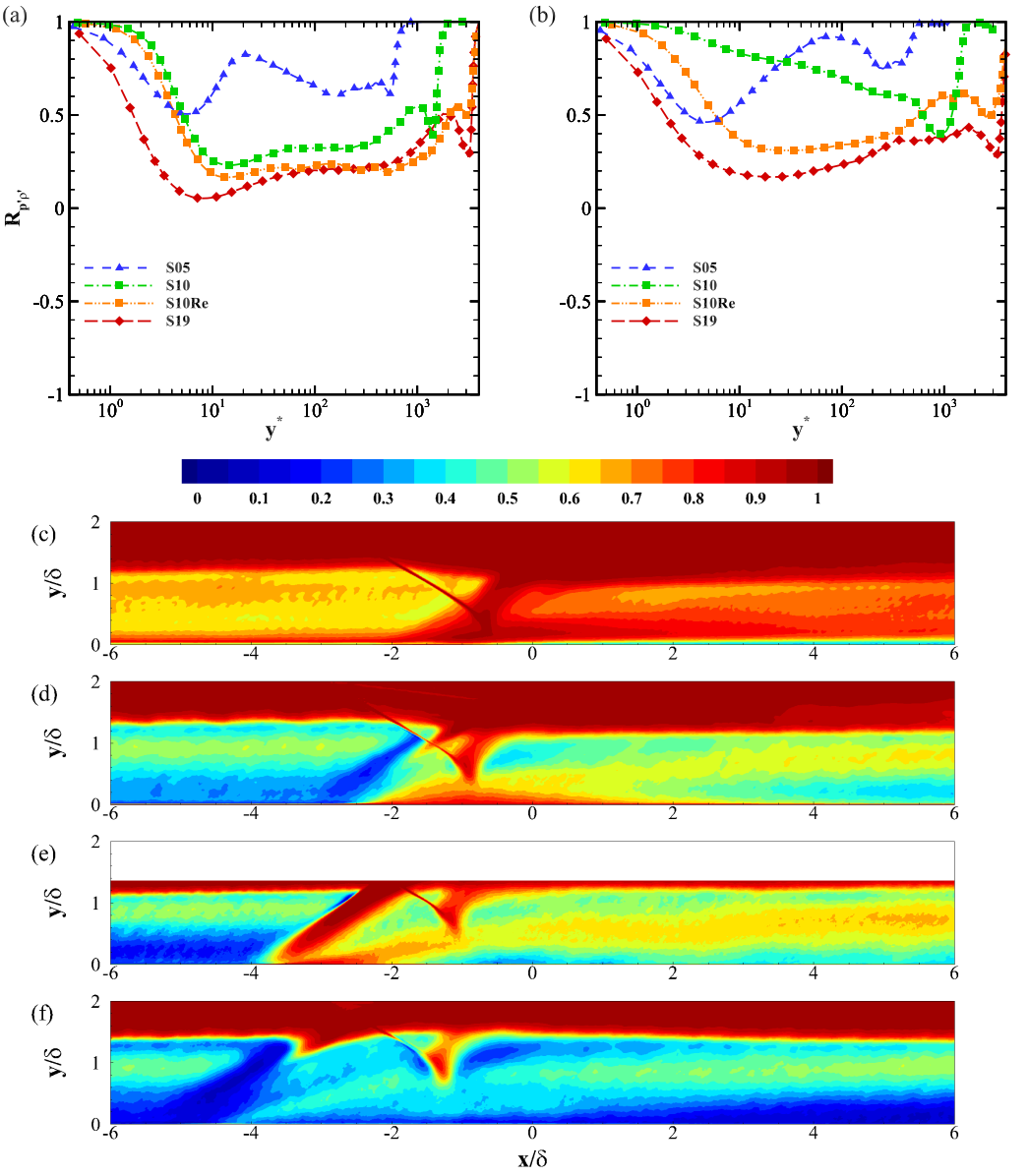

FIG. 10. Distributions of $R_{p'\rho'}$ in (a), (b) inner scaling and (c)–(f) outer scaling. (a) In upstream boundary layer $x = x_{\text{ref}}$; (b) in shock-interaction region $x = x_{\text{imp}}$; (c) case "S05"; (d) case "S10"; (e) case "S10Re"; (f) case "S19".

most sensitive to Ω and Θ. Predictably, in the vicinity of walls with different temperatures, $R_{s'T'}$ differs to a large extent [see Figs. 11(a) and 11(b)], while $R_{s'\rho'}$ is almost the same [see Figs. 12(a) and 12(b)].

The map for $R_{T'\rho'}$ is different from those above, where the neutral line is straight and both the singular points $(\Omega, \Theta) = (1/k_T, -1)$ and $(\Omega, \Theta) = (1/k_\rho, 1)$ function. It is predictable that $R_{T'\rho'}$ differs largely in the vicinity of walls with different temperatures [see Figs. 13(a) and 13(b)]. Since $k_T = \gamma \text{Ma}^2$ is larger than $k_\rho = \gamma(\gamma - 1)\text{Ma}^2$, the neutral line is slightly inclined. As a result,

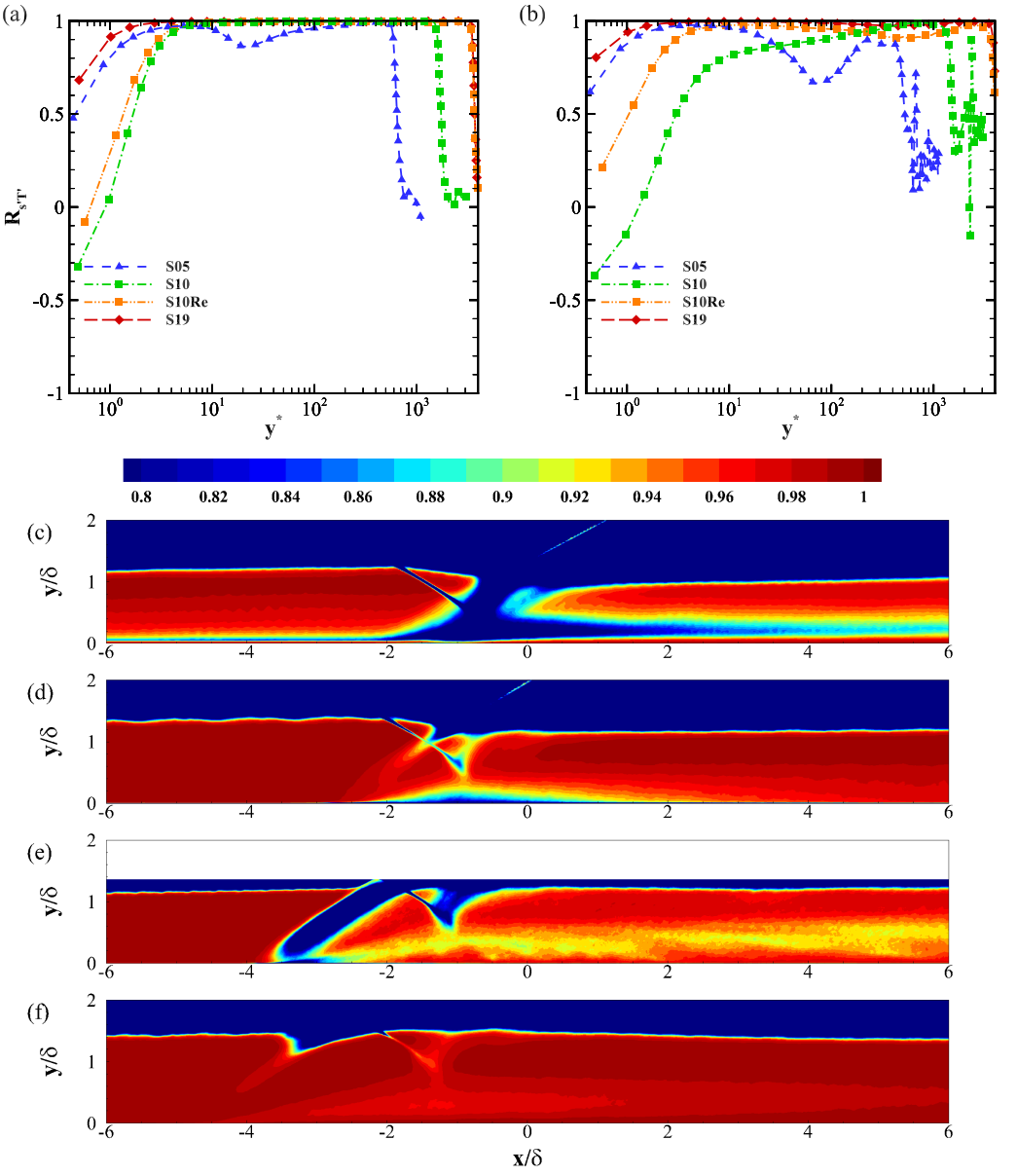

FIG. 11. Distributions of $R_{s'T'}$ in (a), (b) inner scaling and (c)–(f) outer scaling. (a) In upstream boundary layer $x = x_{\text{ref}}$; (b) in shock-interaction region $x = x_{\text{imp}}$; (c) case "S05"; (d) case "S10"; (e) case "S10Re"; (f) case "S19".

positive $R_{T'\rho'}$ is a little more likely to appear when Θ is positive. Moreover, since k_ρ and k_T are larger than unity, the current Ω-Θ space is occupied by mostly negative $R_{T'\rho'}$. This bias is exacerbated as Mach number increases.

In conclusion, with the aid of the maps, the behavior of the correlations between thermodynamic fluctuations in flows with abundant and complicated features can be predicted and explained by analyzing the local Ω and Θ. The effects of wall temperature and Reynolds number on the correlations are also reflected in those on Ω and Θ, as analyzed earlier.

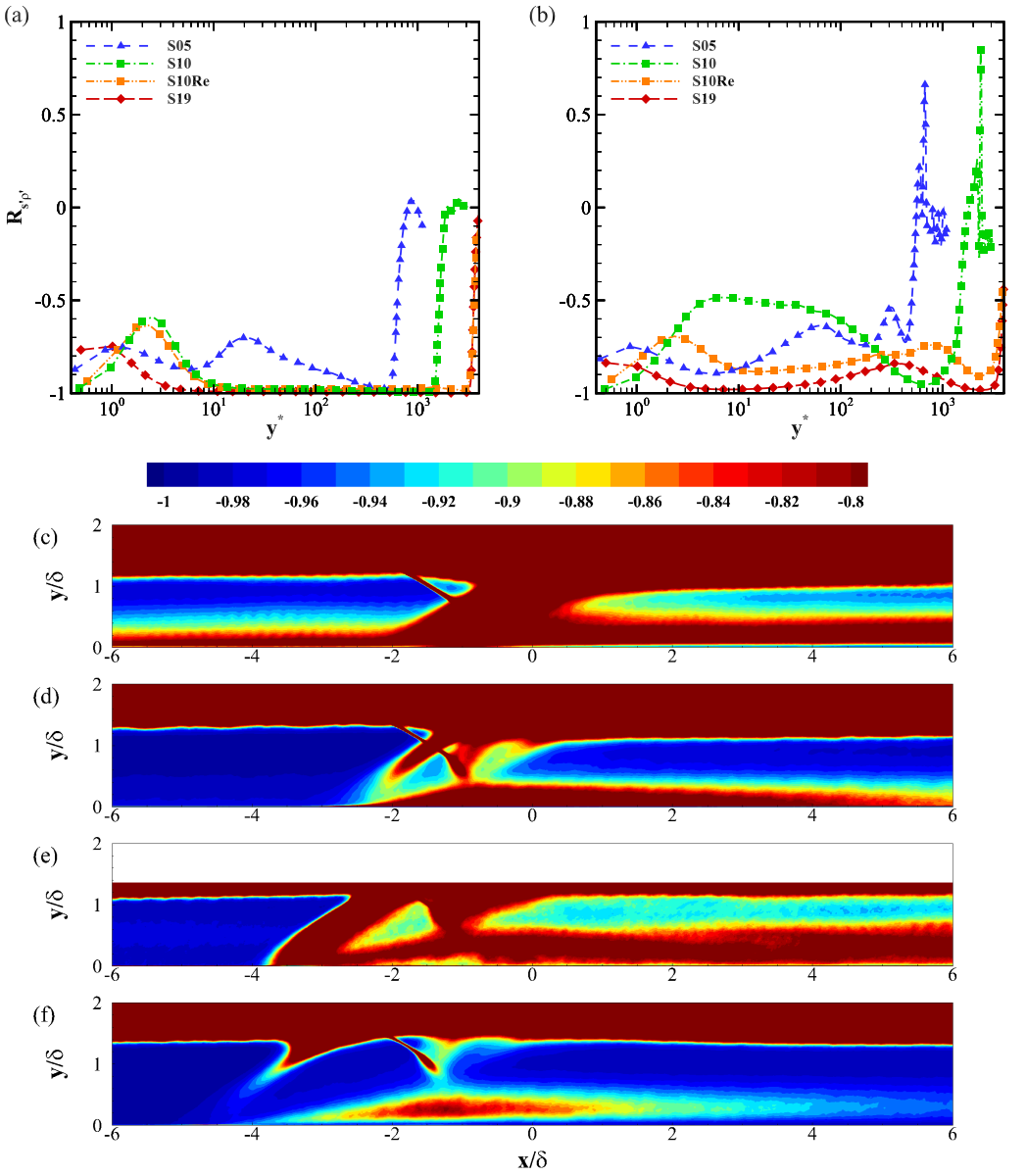

FIG. 12. Distributions of $R_{s'\rho'}$ in (a), (b) inner scaling and (c)–(f) outer scaling. (a) In upstream boundary layer $x = x_{\mathrm{ref}}$; (b) in shock-interaction region $x = x_{\mathrm{imp}}$; (c) case "S05"; (d) case "S10"; (e) case "S10Re"; (f) case "S19".

IV. MODEL FOR THE CORRELATIONS USING R.M.S. VALUES

In Sec. III, the correlations have been shown as functions of Ω and Θ. However, the formulas shown above are too complicated for applications. Besides, one of the variables Θ itself is a second moment correlation, which is difficult to accurately simulate using a coarse grid. Fortunately, it has been shown that Θ is relatively small in a considerable area of the flow, which implies that it could be possible to discard the effect of Θ on the correlations.

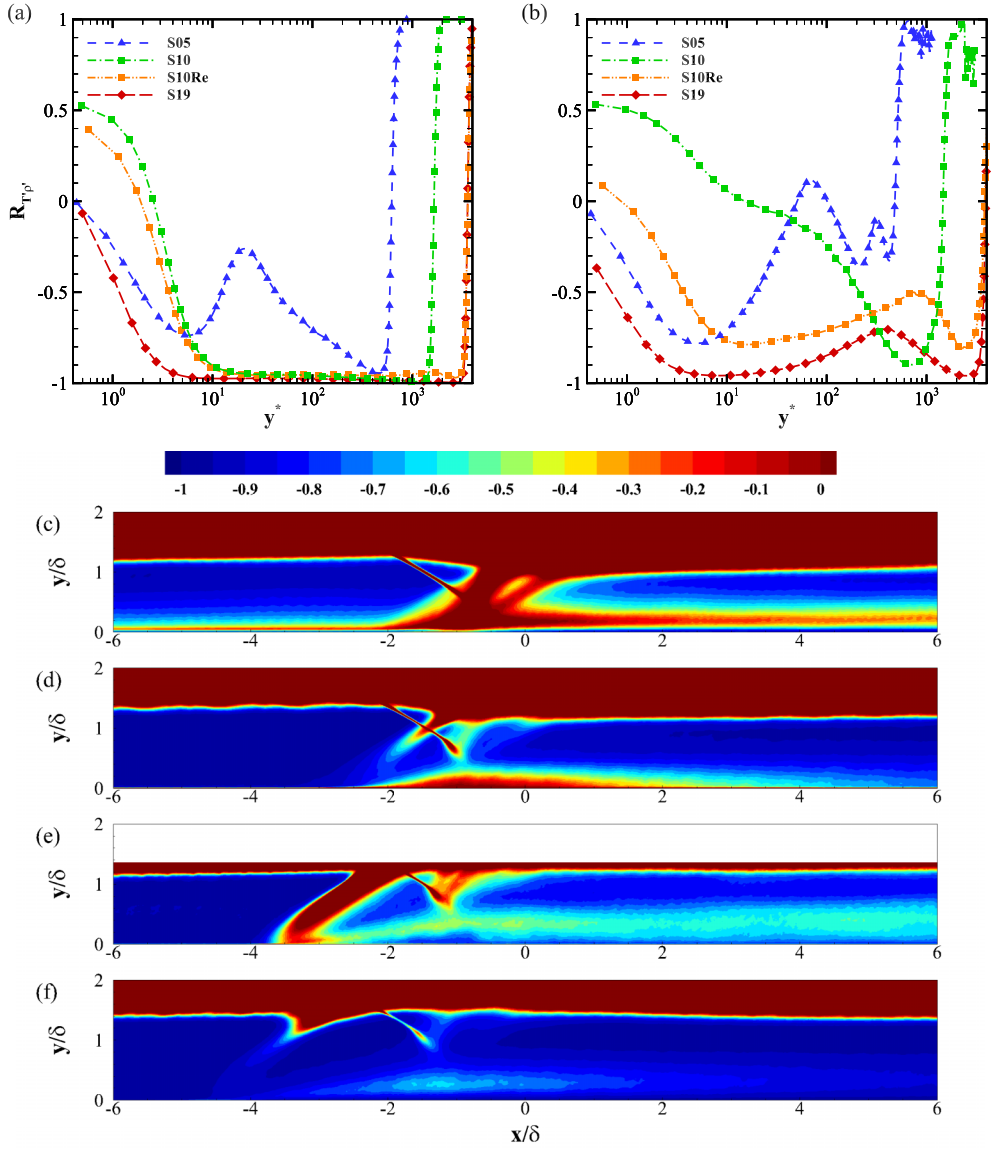

FIG. 13. Distributions of $R_{T'\rho'}$ in (a), (b) inner scaling and (c)–(f) outer scaling. (a) In upstream boundary layer $x = x_{\text{ref}}$; (b) in shock-interaction region $x = x_{\text{imp}}$ (c) case "S05"; (d) case "S10"; (e) case "S10Re"; (f) case "S19".

In this section, we first propose a simplified model for the correlations, which are deemed as functions of merely the r.m.s. levels of the fluctuations, as in Gerolymos and Vallet [20]. Then, the accuracy of the model is examined using DNS data.

A. Derivation of the model

In Eq. (11), the correlations are functions of the r.m.s. values and Θ. However, it should be noted that Θ is a function of three r.m.s. values, according to Eq. (12). To reduce the number of inputs, the influence of Θ has to be eliminated.

Equation (12) also implies the following equations:

$$I_{\rho I}^2 + I_{\rho E}^2 - 2\Theta I_{\rho I} I_{\rho E} - 1 = 0, \tag{14}$$

$$I_{TI}^2 + I_{\mathrm{TE}}^2 + 2\Theta I_{TI} I_{\mathrm{TE}} - 1 = 0. \tag{15}$$

We try to reduce the number of inputs by taking $(10)^2 - (14) \times (15)$ and get

$$R_{\phi'\psi'}^2 = 1 - (1 - \Theta^2)(I_{\phi I} I_{\psi E} \mp I_{\psi I} I_{\phi E})^2, \tag{16}$$

where the minus-plus sign takes positive if ψ' is ρ'. Furthermore, we assume $\Theta^2 \ll 1$ so the $O(\Theta^2)$ term can be discarded, i.e., $R_{\phi'\psi'}^2 \approx 1 - (I_{\phi I} I_{\psi E} \mp I_{\psi I} I_{\phi E})^2$. If we apply the alternative definition of entropic modes mentioned above (just in order to express the coefficients explicitly), Eq. (16) can be rewritten as

$$\begin{aligned}
R_{p's'}^2 &\approx 0, \\
R_{p'T'}^2 &\approx 1 - I_{\mathrm{TE}}^2 = 1 - (\gamma - 1)^2 Ma^4 \frac{s_{\mathrm{rms}}'^2}{(T_{\mathrm{rms}}'/\overline{T})^2}, \\
R_{p'\rho'}^2 &\approx 1 - I_{\rho E}^2 = 1 - (\gamma - 1)^2 Ma^4 \frac{s_{\mathrm{rms}}'^2}{(\rho_{\mathrm{rms}}'/\overline{\rho})^2}, \\
R_{s'T'}^2 &\approx 1 - I_{TI}^2 = 1 - \frac{(\gamma - 1)^2}{\gamma^2} \frac{(p_{\mathrm{rms}}'/\overline{p})^2}{(T_{\mathrm{rms}}'/\overline{T})^2}, \\
R_{s'\rho'}^2 &\approx 1 - I_{\rho I}^2 = 1 - \frac{1}{\gamma^2} \frac{(p_{\mathrm{rms}}'/\overline{p})^2}{(\rho_{\mathrm{rms}}'/\overline{\rho})^2}, \\
R_{T'\rho'}^2 &\approx 1 - (I_{\rho I} I_{\mathrm{TE}} + I_{\rho E} I_{TI})^2 = 1 - (\gamma - 1)^2 Ma^4 \frac{(p_{\mathrm{rms}}'/\overline{p})^2 s_{\mathrm{rms}}'^2}{(T_{\mathrm{rms}}'/\overline{T})^2 (\rho_{\mathrm{rms}}'/\overline{\rho})^2}.
\end{aligned} \tag{17}$$

Accordingly, the magnitudes of the correlations are functions of the normalized r.m.s. values.

From Eq. (17) it can be seen that the number of variables are 2 in $R_{p'T'}$, $R_{p'\rho'}$, $R_{s'T'}$ and $R_{s'\rho'}$. This indicates that a redundant variable in Gerolymos and Vallet [20] is eliminated. The mechanism of the complex interaction between thermodynamic fluctuations becomes clearer as the number of variables is reduced. Interestingly, the p'-involved correlations are functions of s_{rms}', and vice versa. p_{rms}' (or s_{rms}') has only a minor influence on $R_{p'T'}$ and $R_{p'\rho'}$ (or $R_{s'T'}$ and $R_{s'\rho'}$), and the influence is only implicitly functioning in T_{rms}' and ρ_{rms}'.

Note that there are actually three independent variables in $R_{T'\rho'}$, which, in the sense of number of variables, has no advantage over Eq. (11) or the formula proposed by Gerolymos and Vallet [20]. It is retained here for it shares the same form as other formulas.

It should be noted that $R_{p's'}$, although assumed to be weak, is not always negligible in compressible wall-bounded turbulent flows, especially in the vicinity of the wall or near the edge of the boundary layers, as is shown in Sec. III. The validity of Eq. (17) in such regions is questioned and should be examined by DNS data. The validation is in the next subsection. In such regions, we suggest $R_{p's'}$ to be calculated by Eq. (12) instead for higher accuracy.

A weakness of Eq. (17) is that it is capable only of estimating the magnitudes of the correlations. This is not a problem when the variables are strongly correlated, because the signs can be readily obtained, by Eq. (11) or the maps. However, considerable deviations might appear when the correlations are weak. Particularly, the calculated $1 - (I_{\phi I} I_{\psi E} \mp I_{\psi I} I_{\phi E})^2$ might be negative if the correlation is weak, resulting in a complex correlation R. We suggest $R \equiv 0$ if $1 - (I_{\phi I} I_{\psi E} \mp I_{\psi I} I_{\phi E})^2 < 0$.

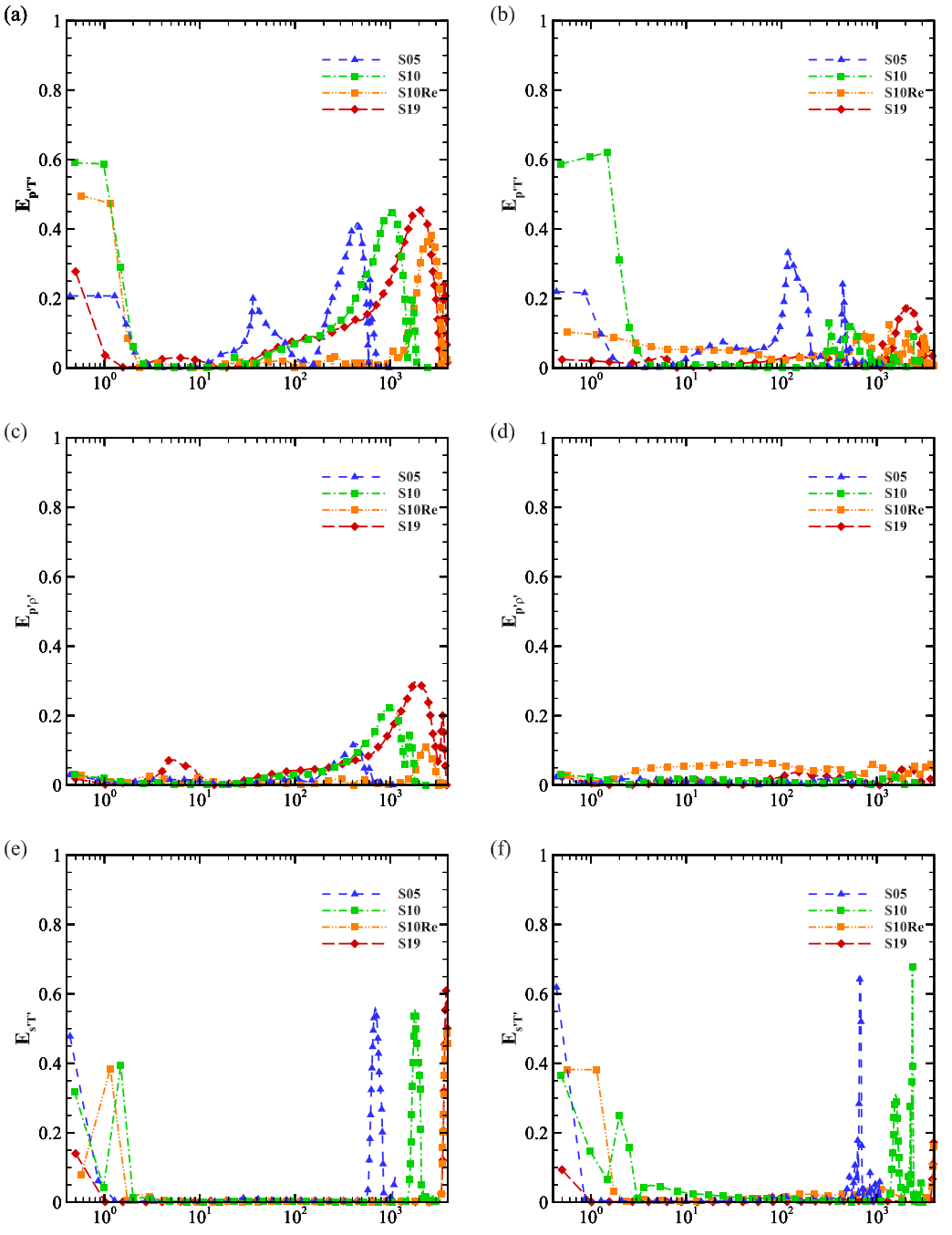

FIG. 14. Profiles of errors (a), (b) $E_{p'T'}$, (c), (d) $E_{p'\rho'}$, (e), (f) $E_{s'T'}$, (g), (h) $E_{s'\rho'}$, and (i), (j) $E_{T'\rho'}$ in inner scaling. On the left (a), (c), (e), (g), (i), in upstream boundary layer $x = x_{\mathrm{ref}}$. On the right (b), (d), (f), (h), (j), in shock-interaction region $x = x_{\mathrm{imp}}$.

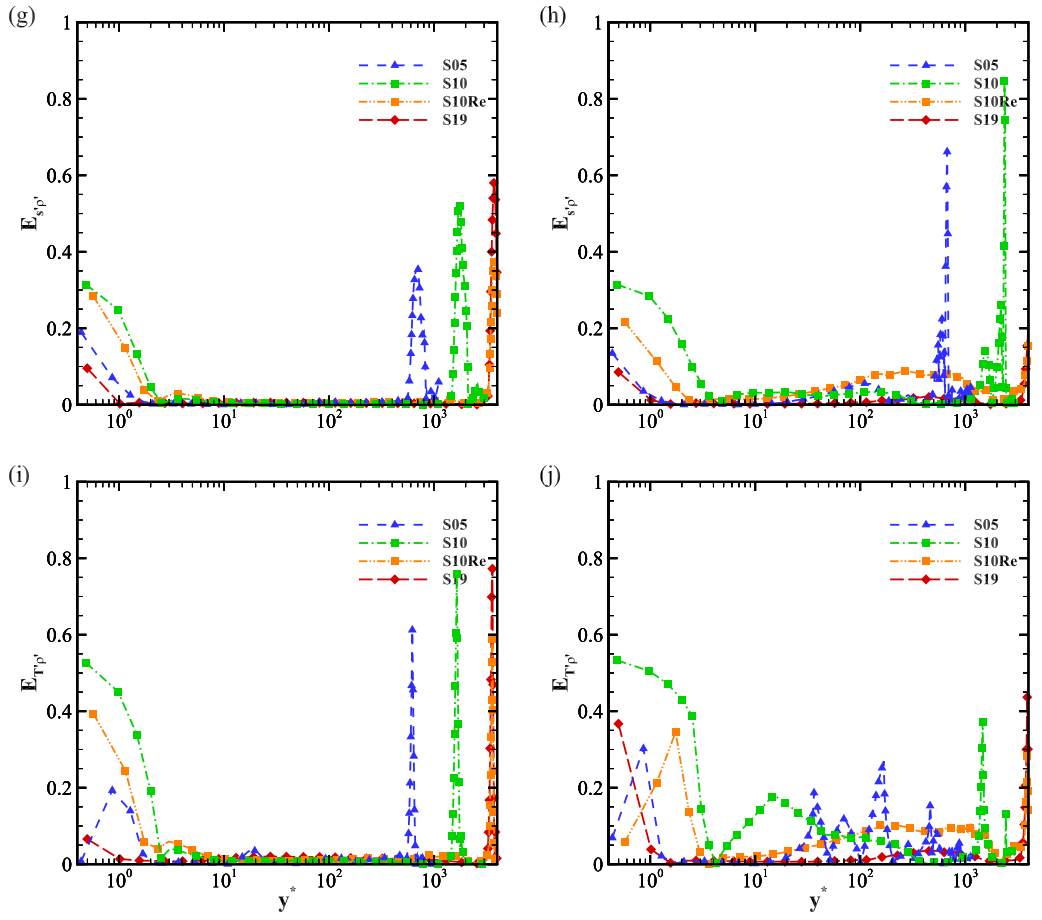

FIG. 14. (*Continued.*)

B. Validation of the model

Since Eq. (17) estimates only the magnitudes of the correlations, we propose the absolute error of absolute correlations $E_{\phi'\psi'} = ||\widehat{R}_{\phi'\psi'}| - |R_{\phi'\psi'}||$ to characterize its validity, where $\widehat{R}_{\phi'\psi'}$ is the estimate calculated by Eq. (17) and $R_{\phi'\psi'}$ is the measurement obtained using DNS data.

As shown in Fig. 7 in Sec. III, the assumption $\Theta^2 \ll 1$ fails to be correct mainly near the edge of the boundary layer and in the vicinity of the wall. Therefore, it is predictable that Eq. (17) loses its validity in such regions. The distributions of errors $E_{p'T'}$, $E_{p'\rho'}$, $E_{s'T'}$, $E_{s'\rho'}$, and $E_{T'\rho'}$ in inner and outer scaling are plotted in Figs. 14 and 15, respectively. Two streamwise locations, $x = x_{\text{ref}}$ and $x = x_{\text{imp}}$, are selected to characterize the flow in the upstream boundary layer and in the shock-interaction region. For results in outer scaling, only those from case "S10" are shown, while those from other cases are similar and omitted for brevity. It can be seen that, in this extremely near-wall layer ($y^* < 2$) mentioned above, the predictions of all five correlations except for $R_{p'\rho'}$ are remarkably deviated from the measurements. Also, there are considerable errors in the predictions for $R_{p'T'}$ and $R_{p'\rho'}$ near the edge of the boundary layer, and in the prediction of $R_{T'\rho'}$ at $y^* = 10 \sim 100$ in the interaction region. Otherwise, the predictions of Eq. (17) are reliable. It should be noted that considerable errors are usually generated where the correlations are quite weak or even change their signs. Therefore, it is acceptable that Eq. (17) is not very accurate in these regions.

It can be seen from Fig. 15(a) that Eq. (17) is valid for $R_{p'T'}$ in the near-wall regions of upstream and reattachment boundary layers (excluding the $y^* < 2$ layer) and in the shock-interaction region.

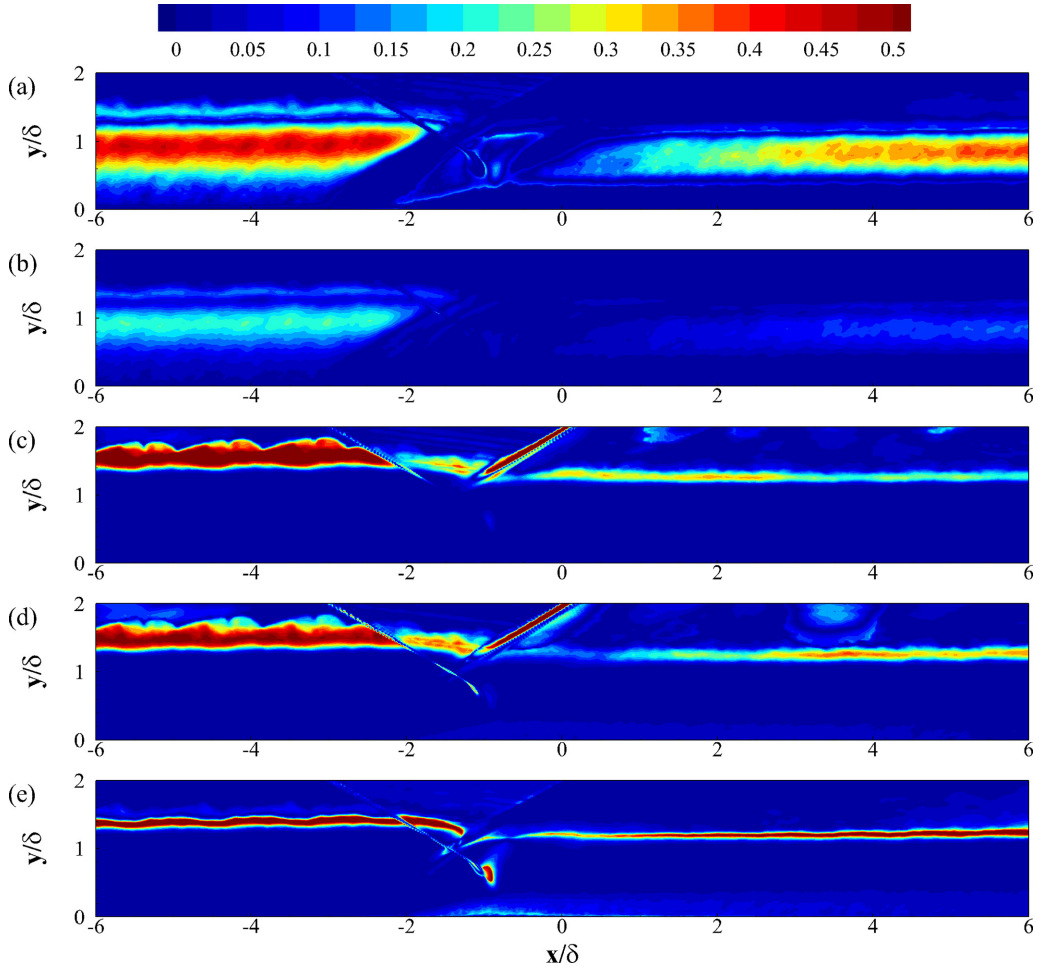

FIG. 15. Distributions of errors (a) $E_{p'T'}$, (b) $E_{p'\rho'}$, (c) $E_{s'T'}$, (d) $E_{s'\rho'}$, and (e) $E_{T'\rho'}$ in the xy plane in outer scaling. Only results from case "S10" are shown.

The error is up to 0.45 near the edges of the upstream and reattachment boundary layers, which may be a direct result of the failure of assumption $\Theta^2 \ll 1$, and further results from TNTI. The distribution of $E_{p'\rho'}$, shown in Fig. 15(b), is similar to that of $E_{p'T'}$. The error is up to 0.2, indicating higher accuracy of Eq. (17) for $R_{p'\rho'}$ than for $R_{p'T'}$. It can be seen from Figs. 15(c) and 15(d) that Eq. (17) has an even higher accuracy for $R_{s'T'}$ and $R_{s'\rho'}$, with the error less than 0.05. The validity for these two correlations is verified in the whole boundary layer. Figure 15(e) shows that except near the tip of the incident shock or in the separation bubble, the estimation of $R_{T'\rho'}$ is also quite accurate, with the error less than 0.05. In conclusion, Eq. (17) is valid in most of the regions inside the boundary layer, except for a very limited area where $\Theta^2 \ll 1$ fails. Since errors in the shock-interaction region are not larger than those in upstream boundary layer, it can be inferred that our model is applicable in not only SWBLI flows but also other compressible wall-bounded flows.

V. CONCLUDING REMARKS

In this paper, the second moment correlations between thermodynamic fluctuations in shock wave/turbulent boundary layer interaction is systematically investigated. DNSs of three isothermal wall conditions and two friction Reynolds numbers are conducted.

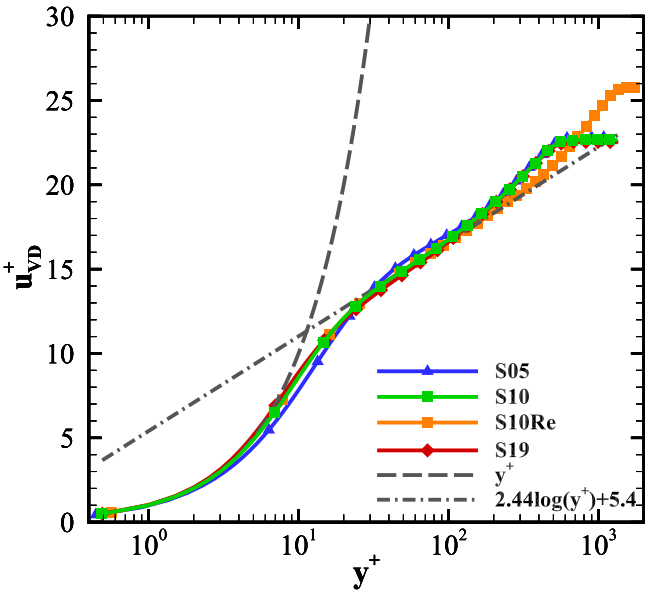

FIG. 16. Van Driest transformed velocity profile at x_{ref}.

Based on Kovásznay decomposition, an approach is proposed to quantitatively characterize the contributing factors to the correlations. It is shown that all six concerned correlations are determined by merely two parameters, which are interpreted as intermodal competition and intermodal correlation, respectively. The effects of wall temperature and Reynolds number on the two parameters are different. According to the modal intensities, the flow field is divided into several zones, each with distinct physical properties. The two parameters vary to a large extent in different zones of the flow. By analyzing the local parameters, the behavior of the correlations affected by complicated flow features can be predicted and explained.

In addition, a simplified model is proposed where the correlations are deemed as functions of the r.m.s. values of thermodynamic fluctuations. The model is much simpler than that in previous studies. The formula for each correlation has the same form. The accuracy of the model is validated in boundary layers where the intermodal correlation is weak.

In this paper, the correlations between thermodynamic fluctuations are investigated. The underlying physical mechanisms are revealed. A practical model is proposed. The main limit in our study is limited parameter space. The effects of Mach number and wedge angle are left for future studies. It would also be interesting to investigate the near-wall correlations without strictly isothermo wall conditions or the correlations near rough walls.

ACKNOWLEDGMENTS

This work was supported by National Natural Science Foundation of China (NSFC Grants No. 12172161, No. 12161141017, No. 92052301, and No. 91952104), by the NSFC Basic Science Center Program (Grant No. 11988102), by the Technology and Innovation Commission of Shenzhen Municipality (Grants No. KQTD20180411143441009 and No. JCYJ20170412151759222), and by the Department of Science and Technology of Guangdong Province (Grants No. 2019B21203001, No. 2020B1212030001, and No. 2023B1212060001). This work was also supported by the Center for Computational Science and Engineering of Southern University of Science and Technology.

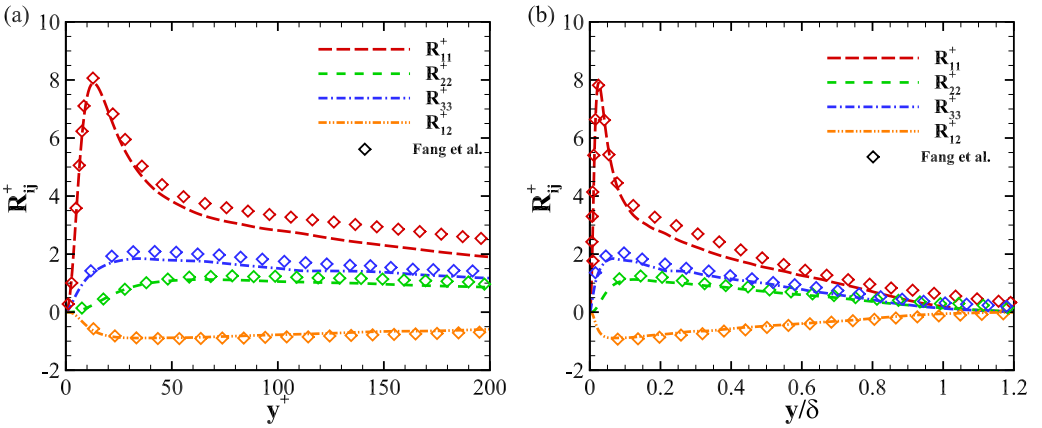

FIG. 17. Density-scaled Reynolds stresses R_{ij}^+ in (a) inner scaling and (b) outer scaling.

APPENDIX: VALIDATION OF THE DNS DATABASE

To validate the accuracy of the database, the van Driest transformed velocity profile at reference station is shown in Fig. 16. The profile performs a linear scaling at $y^+ < 5$ and a logarithmic scaling at $30 < y^+ < 150$ (the range is $30 < y^+ < 300$ for case "S10Re"). Moreover, the density-scaled Reynolds stresses $R_{ij}^+ = \overline{\rho}\widetilde{u_i''u_j''}^+/\overline{\rho}_w$ in inner and outer scaling at x_{ref} are plotted in Fig. 17, respectively. For brevity, only results in the adiabatic cases are shown. The results are compared with those of supersonic data by Fang *et al.* [11]. The difference is small in most of the regions in the boundary layer.

Besides, Fig. 18 shows the streamwise distribution of $p_w^* = (\overline{p}_w - p_\infty)/(p_1 - p_\infty)$, averaged wall pressure normalized as suggested by Fang *et al.* [11], where p_1 is the far-field pressure downstream of the incident shock. Results in all the cases are shown, of which results in case

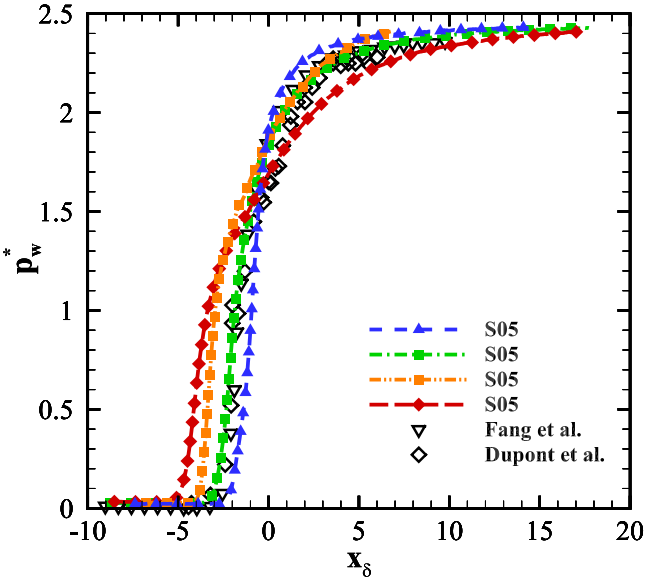

FIG. 18. Normalized wall pressure.

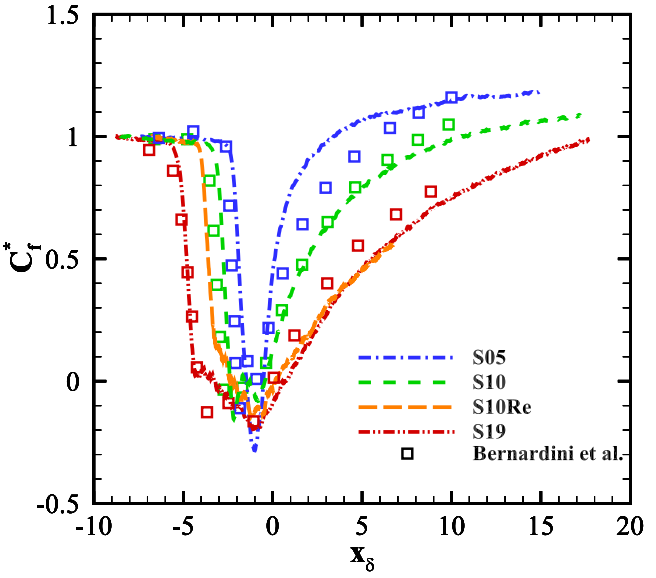

FIG. 19. Normalized skin friction coefficient.

"S10" are compared with the measurement of Dupont *et al.* [53] and the simulation of Fang *et al.* [11]. Qualitative agreements are achieved between our database and the two references. Figure 19 represents the normalized skin friction coefficient $C_f^* = C_f/C_{f,\mathrm{ref}}$, where $C_f = 2\tau_w/\rho_\infty u_\infty^2$. The curves are compared with those of Bernardini *et al.* [25]. The trends of the curves are similar, and the separation lengths are comparable. A minor quantitative difference can be ascribed to different Reynolds numbers and wall boundary conditions. The Reynolds number effect on C_f^* is consistent with Volpiani *et al.* [26].

[1] M. Holden, A review of aerothermal problems associated with hypersonic flight, in *24th Aerospace Sciences Meeting*, Reno, NV (AIAA, 1986).

[2] P. P. Doerffer and R. Bohning, Shock wave–boundary layer interaction control by wall ventilation, Aerosp. Sci. Technol. **7**, 171 (2003).

[3] H. Babinsky and J. K. Harvey, *Shock Wave-Boundary-Layer Iinteractions* (Cambridge University Press, Cambridge, UK, 2011), Vol. 32.

[4] T. Adamson Jr. and A. Messiter, Analysis of two-dimensional interactions between shock waves and boundary layers, Annu. Rev. Fluid Mech. **12**, 103 (1980).

[5] Y. Andreopoulos, J. H. Agui, and G. Briassulis, Shock wave–turbulence interactions, Annu. Rev. Fluid Mech. **32**, 309 (2000).

[6] N. T. Clemens and V. Narayanaswamy, Low-frequency unsteadiness of shock wave/turbulent boundary layer interactions, Annu. Rev. Fluid Mech. **46**, 469 (2014).

[7] D. V. Gaitonde and M. C. Adler, Dynamics of three-dimensional shock-wave/boundary-layer interactions, Annu. Rev. Fluid Mech. **55**, 291 (2023).

[8] D. S. Dolling, Fifty years of shock-wave/boundary-layer interaction research: What next? AIAA J. **39**, 1517 (2001).

[9] M. Mustafa, N. Parziale, M. Smith, and E. Marineau, Amplification and structure of streamwise-velocity fluctuations in compression-corner shock-wave/turbulent boundary-layer interactions, J. Fluid Mech. **863**, 1091 (2019).

[10] S. Pirozzoli and F. Grasso, Direct numerical simulation of impinging shock wave/turbulent boundary layer interaction at $M = 2.25$, Phys. Fluids **18**, 065113 (2006).
[11] J. Fang, A. A. Zheltovodov, Y. Yao, C. Moulinec, and D. R. Emerson, On the turbulence amplification in shock-wave/turbulent boundary layer interaction, J. Fluid Mech. **897**, A32 (2020).
[12] M. Yu, S. Dong, P. Liu, Z. Tang, X. Yuan, and C. Xu, Post-shock turbulence recovery in oblique-shock/turbulent boundary layer interaction flows, J. Fluid Mech. **961**, A26 (2023).
[13] T. Guo, J. Zhang, F. Tong, and X. Li, Amplification of turbulent kinetic energy and temperature fluctuation in a hypersonic turbulent boundary layer over a compression ramp, Phys. Fluids **35**, 046118 (2023).
[14] F.-Y. Zuo, Hypersonic shock wave/turbulent boundary layer interaction over a compression ramp, AIAA J. **61**, 1579 (2023).
[15] A. Hadjadj, Large-eddy simulation of shock/boundary-layer interaction, AIAA J. **50**, 2919 (2012).
[16] A. Gross, P. Castillo Gomez, and S. Lee, Wall-modeled large-eddy simulations of turbulent shockwave boundary layer interaction and boundary layer flows, in *AIAA Aviation 2021 Forum*, Virtual Event (AIAA, 2021).
[17] D. Taulbee and J. VanOsdol, Modeling turbulent compressible flows–The mass fluctuating velocity and squared density, in *29th Aerospace Sciences Meeting*, Reno, NV (AIAA, 1991).
[18] L. Wei and A. Pollard, Interactions among pressure, density, vorticity and their gradients in compressible turbulent channel flows, J. Fluid Mech. **673**, 1 (2011).
[19] G. Gerolymos and I. Vallet, Pressure, density, temperature and entropy fluctuations in compressible turbulent plane channel flow, J. Fluid Mech. **757**, 701 (2014).
[20] G. Gerolymos and I. Vallet, Correlation coefficients of thermodynamic fluctuations in compressible aerodynamic turbulence, J. Fluid Mech. **851**, 447 (2018).
[21] D. Xu, J. Wang, and S. Chen, Reynolds number and wall cooling effects on correlations between the thermodynamic variables in hypersonic turbulent boundary layers, J. Fluid Mech. **965**, A4 (2023).
[22] N. A. Adams, Direct simulation of the turbulent boundary layer along a compression ramp at $M = 3$ and $Re_\theta = 1685$, J. Fluid Mech. **420**, 47 (2000).
[23] L. S. Kovasznay, Turbulence in supersonic flow, J. Aeronaut. Sci. **20**, 657 (1953).
[24] V. Jaunet, J. Debiève, and P. Dupont, Length scales and time scales of a heated shock-wave/boundary-layer interaction, AIAA J. **52**, 2524 (2014).
[25] M. Bernardini, I. Asproulias, J. Larsson, S. Pirozzoli, and F. Grasso, Heat transfer and wall temperature effects in shock wave turbulent boundary layer interactions, Phys. Rev. Fluids **1**, 084403 (2016).
[26] P. S. Volpiani, M. Bernardini, and J. Larsson, Effects of a nonadiabatic wall on supersonic shock/boundary-layer interactions, Phys. Rev. Fluids **3**, 083401 (2018).
[27] X.-K. Zhu, C.-P. Yu, F.-L. Tong, and X.-L. Li, Numerical study on wall temperature effects on shock wave/turbulent boundary-layer interaction, AIAA J. **55**, 131 (2017).
[28] D. Exposito, S. Gai, and A. Neely, Wall temperature and bluntness effects on hypersonic laminar separation at a compression corner, J. Fluid Mech. **922**, A1 (2021).
[29] S. Dong, F. Tong, M. Yu, J. Chen, X. Yuan, and Q. Wang, Effects of wall temperature on two-point statistics of the fluctuating wall shear stress and heat flux in supersonic turbulent boundary layers, Phys. Fluids **34**, 065114 (2022).
[30] F.-Y. Zuo, J.-R. Wei, S.-L. Hu, and S. Pirozzoli, Effects of wall temperature on hypersonic impinging shock-wave/turbulent-boundary-layer interactions, AIAA J. **60**, 5109 (2022).
[31] J. Wang, M. Wan, S. Chen, C. Xie, L.-P. Wang, and S. Chen, Cascades of temperature and entropy fluctuations in compressible turbulence, J. Fluid Mech. **867**, 195 (2019).
[32] X. Li, D. Fu, Y. Ma, and X. Liang, Direct numerical simulation of shock/turbulent boundary layer interaction in a supersonic compression ramp, Sci. China Phys. Mech. Astron. **53**, 1651 (2010).
[33] D. Xu, J. Wang, C. Yu, X. Li, and S. Chen, Effect of compressibility on the small-scale structures in hypersonic turbulent boundary layer, Phys. Fluids **34**, 055121 (2022).
[34] D. Xu, J. Wang, C. Yu, X. Li, and S. Chen, Contribution of flow topology to the kinetic energy flux in hypersonic turbulent boundary layer, Phys. Fluids **34**, 046103 (2022).
[35] F. Tong, Z. Tang, C. Yu, X. Zhu, and X. Li, Numerical analysis of shock wave and supersonic turbulent boundary interaction between adiabatic and cold walls, J. Turbul. **18**, 569 (2017).

[36] F. Tong, C. Yu, Z. Tang, and X. Li, Numerical studies of shock wave interactions with a supersonic turbulent boundary layer in compression corner: Turning angle effects, Comput. Fluids **149**, 56 (2017).
[37] F. Tong, J. Duan, and X. Li, Shock wave and turbulent boundary layer interaction in a double compression ramp, Comput. Fluids **229**, 105087 (2021).
[38] F. Tong, X. Yuan, J. Lai, J. Duan, D. Sun, and S. Dong, Wall heat flux in a supersonic shock wave/turbulent boundary layer interaction, Phys. Fluids **34**, 065104 (2022).
[39] F. Tong, J. Duan, and X. Li, Characteristics of reattached boundary layer in shock wave and turbulent boundary layer interaction, Chin. J. Aeronaut. **35**, 172 (2022).
[40] F. Tong, J. Lai, J. Duan, S. Dong, X. Yuan, and X. Li, Effect of interaction strength on recovery downstream of incident shock interactions, Phys. Fluids **34**, 125127 (2022).
[41] D. S. Balsara and C.-W. Shu, Monotonicity preserving weighted essentially non-oscillatory schemes with increasingly high order of accuracy, J. Comput. Phys. **160**, 405 (2000).
[42] J. Duan, F. Tong, X. Li, and H. Liu, Decomposition of mean skin friction in incident shock wave/turbulent boundary layer interaction flows at Mach 2.25, Chin. J. Aeronaut. **36**, 178 (2023).
[43] L. Duan, I. Beekman, and M. Martin, Direct numerical simulation of hypersonic turbulent boundary layers. Part 2. Effect of wall temperature, J. Fluid Mech. **655**, 419 (2010).
[44] F. W. Spaid and J. C. Frishett, Incipient separation of a supersonic, turbulent boundary layer, including effects of heat transfer, AIAA J. **10**, 915 (1972).
[45] D. Xu, J. Wang, M. Wan, C. Yu, X. Li, and S. Chen, Compressibility effect in hypersonic boundary layer with isothermal wall condition, Phys. Rev. Fluids **6**, 054609 (2021).
[46] M. Bernardini, G. Della Posta, F. Salvadore, and E. Martelli, Unsteadiness characterisation of shock wave/turbulent boundary-layer interaction at moderate Reynolds number, J. Fluid Mech. **954**, A43 (2023).
[47] P. Huang, G. N. Coleman, and P. Bradshaw, Compressible turbulent channel flows: DNS results and modelling, J. Fluid Mech. **305**, 185 (1995).
[48] M. Yu, D. Sun, Q. Zhou, P. Liu, and X. Yuan, Coherent structures and turbulent model refinement in oblique shock/hypersonic turbulent boundary layer interactions, Phys. Fluids **35**, 086125 (2023).
[49] J. A. Sillero, J. Jiménez, and R. D. Moser, Two-point statistics for turbulent boundary layers and channels at Reynolds numbers up to $\delta^+ \approx 2000$, Phys. Fluids **26**, 105109 (2014).
[50] B.-T. Chu and L. S. Kovásznay, Non-linear interactions in a viscous heat-conducting compressible gas, J. Fluid Mech. **3**, 494 (1958).
[51] P. Chassaing, R. Antonia, F. Anselmet, L. Joly, and S. Sarkar, *Variable Density Fluid Turbulence, Fluid Mechanics and Its Applications* (Springer, Dordrecht, 2002).
[52] S. Gauthier, Compressible Rayleigh–Taylor turbulent mixing layer between Newtonian miscible fluids, J. Fluid Mech. **830**, 211 (2017).
[53] P. Dupont, C. Haddad, and J. Debieve, Space and time organization in a shock-induced separated boundary layer, J. Fluid Mech. **559**, 255 (2006).